Mean State AMOC Affects AMOC Weakening through Subsurface Warming in the Labrador Sea

YUAN-JEN LIN,[a,b] BRIAN E. J. ROSE,[b] AND YEN-TING HWANG[a]

[a] *Department of Atmospheric Sciences, National Taiwan University, Taipei, Taiwan*
[b] *Department of Atmospheric and Environmental Sciences, University at Albany, State University of New York, Albany, New York*

(Manuscript received 23 June 2022, in final form 9 February 2023, accepted 15 February 2023)

ABSTRACT: While most models agree that the Atlantic meridional overturning circulation (AMOC) becomes weaker under greenhouse gas emission and is likely to weaken over the twenty-first century, they disagree on the projected magnitudes of AMOC weakening. In this work, CMIP6 models with stronger climatological AMOC are shown to project stronger AMOC weakening in both 1% ramping CO_2 and abrupt CO_2 quadrupling simulations. A physical interpretation of this result is developed. For models with stronger mean state AMOC, stratification in the upper Labrador Sea is weaker, allowing for stronger mixing of the surface buoyancy flux. In response to CO_2 increase, surface warming is mixed to the deeper Labrador Sea in models with stronger upper-ocean mixing. This subsurface warming and corresponding density decrease drives AMOC weakening through advection from the Labrador Sea to the subtropics via the deep western boundary current. Time series analysis shows that most CMIP6 models agree that the decrease in subsurface Labrador Sea density leads AMOC weakening in the subtropics by several years. Also, idealized experiments conducted in an ocean-only model show that the subsurface warming over 500–1500 m in the Labrador Sea leads to stronger AMOC weakening several years later, while the warming that is too shallow (<500 m) or too deep (>1500 m) in the Labrador Sea causes little AMOC weakening. These results suggest that a better representation of mean state AMOC is necessary for narrowing the intermodel uncertainty of AMOC weakening to greenhouse gas emission and its corresponding impacts on future warming projections.

KEYWORDS: Meridional overturning circulation; Ocean dynamics; Climate models

1. Introduction

The Atlantic meridional overturning circulation (AMOC) is a global ocean circulation that generally transports warm and salty upper waters northward, releasing heat to the atmosphere to form the cold, deep waters flowing southward. The AMOC varies over broad time scales, and these AMOC variations shape global and regional climate through the transport of heat, salt, and biochemical substances (Jackson et al. 2015; Liu et al. 2020; Zhang et al. 2019). The climate impacts associated with the time-evolving AMOC include changes in sea surface temperature (Knight et al. 2005; Muir and Fedorov 2015), shifts in tropical precipitation (Moreno-Chamarro et al. 2019; Parsons et al. 2014), the extent of the Arctic sea ice (Liu and Fedorov 2019; Mahajan et al. 2011), and projections of sea level rise (Gregory et al. 2016; Little et al. 2019).

Since the AMOC plays a vital role in modifying the global climate, scientists have been focusing on the driving mechanisms of the AMOC variations on multiple time scales. On seasonal to interannual time scale, wind stress curl can drive the Ekman transport that corresponds to meridional Sverdrup flow (Eden and Willebrand 2001; Köhl 2005). At the same time, surface wind forcing might trigger Rossby waves that modify the basinwide east–west density gradient (Hirschi et al. 2007). Both account for the higher-frequency AMOC fluctuations (Zhao and Johns 2014). On interannual to decadal time scale, buoyancy flux plays a major role in determining the AMOC variations (Yeager and Robson 2017). Studies have found that the North Atlantic Oscillation (NAO) may be responsible for the decadal buoyancy forcing in the subpolar region (Delworth and Zeng 2016; Eden and Jung 2001; Lohmann et al. 2009), and the transport of the buoyancy anomalies involves multiple processes including mean ocean advection and propagation via boundary waves (Buckley and Marshall 2016; Zhang 2010). On centennial to millennial time scales, water flux and the associated salinity anomalies become dominant in changing the AMOC strength (Delworth and Zeng 2012; Menary et al. 2012).

Besides understanding the driving mechanisms of AMOC variations on a broad range of time scales, it is as important to evaluate the anthropogenically forced AMOC responses and to predict the future AMOC changes. Due to the relatively sparse and short period of direct AMOC observation since 2004 (Smeed et al. 2014, 2018), it is still unclear if the recently observed AMOC weakening is a forced response to greenhouse gas emissions or is instead due to internal variability (Jackson et al. 2016; Menary et al. 2020; Worthington et al. 2021). To understand how the AMOC would respond to anthropogenic forcing, we usually rely on numerical models, which commonly show that the AMOC weakens in response to increasing CO_2 and most of them also project a long-term

Denotes content that is immediately available upon publication as open access.

Supplemental information related to this paper is available at the Journals Online website: https://doi.org/10.1175/JCLI-D-22-0464.s1.

Corresponding author: Yen-Ting Hwang, ythwang@ntu.edu.tw

DOI: 10.1175/JCLI-D-22-0464.1

AMOC weakening over the twenty-first century (IPCC 2013, 2021; Weijer et al. 2020).

Multiple features under a warmer future may be linked to the projected AMOC weakening. For example, reduced ocean heat loss at high latitudes (Drijfhout et al. 2014), increased precipitation in the North Atlantic (Dima et al. 2021), Arctic sea ice loss (Liu et al. 2019; Sévellec et al. 2017), and Greenland ice sheet melting (Bakker et al. 2016; Hu et al. 2011; Swingedouw et al. 2006). Though the ultimate cause for the AMOC weakening remains an open question, some studies show that the surface heat flux anomalies account for the AMOC weakening under increasing CO_2, outweighing the role of water flux or momentum flux (Gregory et al. 2005, 2016). Also, some show that the AMOC weakening over the twenty-first century or in response to freshwater forcing is mostly through reduced density from warming instead of freshening (Haskins et al. 2020; Levang and Schmitt 2020).

While the models qualitatively agree on the sign of AMOC weakening in response to CO_2 increase, they disagree on the projected magnitudes (IPCC 2021; Reintges et al. 2017). The large intermodel spread of AMOC weakening magnitudes can bring uncertainties in a broad range of future projections (Bellomo et al. 2021; Hu et al. 2020). Some studies have found that the magnitudes of the AMOC weakening depend on the mean state AMOC strength—the models with stronger mean state AMOC usually correspond to more significant AMOC weakening under CO_2 increase (Gregory et al. 2005; Jackson et al. 2020; Weaver et al. 2012; Weijer et al. 2020; Winton et al. 2014). The findings suggest that the present-day AMOC strength could be an emergent constraint for projected AMOC weakening. However, explanations for the diverse magnitudes of AMOC weakening among models and their dependence on the mean state climate are not fully understood.

In this work, we provide processes to interpret the spread of model projections of AMOC weakening and its dependence on the mean state climate. We begin by showing the climatological and projected AMOC strength, as well as the mean state climate in the North Atlantic in fully coupled climate models (section 2). In section 3, we analyze surface responses related to the model-dependent AMOC weakening. In section 4, we develop a process-based understanding of the dependence of AMOC weakening on the climatological AMOC strength. We find that the subsurface warming in the Labrador Sea acts as a precursor to AMOC weakening in most models, and the varying vertical warming profiles in the Labrador Sea are linked to their varying mean state stratification. In section 5, we perform idealized experiments, suggesting that the subsurface warming in the Labrador Sea leads to stronger AMOC weakening than warming in the upper or deep ocean. The proposed mechanisms are summarized in section 6, along with the discussion of the related literature.

2. Mean state climate and AMOC weakening

a. CMIP6 models data

We use 31 models participating in phase 6 of the Climate Model Intercomparison Project (CMIP6; summarized in Table 1) and analyze their monthly output from 150-yr simulations with preindustrial conditions (piControl) and forced with an increase in atmospheric CO_2 concentration, including the scenario in which CO_2 increases at 1% yr^{-1} (1pctCO_2) and the scenario in which CO_2 abruptly quadruples at the start of the simulation and is subsequently held fixed (abrupt-4×CO_2). To evaluate the potential density responses in each model, the criterion for choosing the models is the availability of seawater potential temperature (thetao) and salinity (so) in all three simulations. Here we calculate the potential density following the Thermodynamic Equation of Seawater-2010 (TEOS-10) (IOC et al. 2010). When available, we also analyze sea ice cover and surface heat budget. To evaluate the AMOC strength, we make use of mass overturning streamfunctions and meridional velocity (see the appendix for more details). Only one ensemble member per model is assessed, as most of the models provided only one member.

b. Dependence of AMOC weakening on AMOC climatology

Similar to CMIP3 and CMIP5, the 31 CMIP6 models used in the study show a considerable intermodel spread of climatological AMOC strength, ranging from 11 to 28 Sv (1 Sv ≡ 10^6 m^3 s^{-1}) (Fig. 1a). Here we define the AMOC strength as the mass streamfunctions at 35°N and 1000-m depth, where the maximum is generally located. The large intermodel spread of AMOC climatology not only leads to model biases in mean state climate (Wang et al. 2014) but also accounts for the uncertainties in future projections (Chen et al. 2019). For example, the amplitude of AMOC weakening depends on the strength of AMOC climatology in both abrupt-4×CO_2 and 1pctCO_2 simulations—the models with stronger AMOC mean state tend to project stronger AMOC weakening (Figs. 1b,c). The Spearman correlation coefficient between the AMOC climatological strength and the magnitude of AMOC weakening in years 11–30 of abrupt-4×CO_2 simulations is 0.87 (p value = 0.000), and 0.54 (p value = 0.002) for years 131–150 of 1pctCO_2 simulations. While there is a significant correlation between the AMOC climatology and the absolute magnitudes of the AMOC changes, we find that the percentage change of the AMOC is less significantly correlated with the AMOC climatology in abrupt-4×CO_2 simulations, and there is no significant correlation for 1pctCO_2 simulations.

To study the AMOC mean state control on AMOC weakening, we compare results from the 10 (out of 31) models that have the strongest AMOC mean state (hereafter S10; in red) with the 10 models that have the weakest AMOC mean state (hereafter W10; in blue). The mean value (one standard deviation) of AMOC climatology from S10 and W10 is 24.4 (2.1) and 15.9 (2.5) Sv, respectively. Under CO_2 forcing, the difference of 8.5 Sv in AMOC strength between the two groups becomes smaller, since S10 models project stronger AMOC weakening and W10 models project weaker AMOC weakening (Figs. 1b,c). Indeed, the years 11–30 mean AMOC strength difference in the abrupt-4×CO_2 simulation between S10 and W10 is only 1.9 Sv, and the years 131–150 mean AMOC strength difference in the 1pctCO_2 simulation is 3.2 Sv (Fig. 1a). The dependence of the AMOC weakening on

TABLE 1. The 31 CMIP6 models used in the study.

Institution	Model name	References
CSIRO-ARCCSS	ACCESS-CM2	Dix et al. (2019a,b,c)
CSIRO	ACCESS-ESM1-5	Ziehn et al. (2019a,b,c)
BCC	BCC-CSM2-MR	Wu et al. (2018a,b,c)
BCC	BCC-ESM1	Zhang et al. (2018, 2019a,b)
CAMS	CAMS-CSM1-0	Rong (2019a,b,c)
CAS	CAS-ESM2-0	Chai (2020a,b,c)
NCAR	CESM2	Danabasoglu (2019a,b); Danabasoglu et al. (2019)
NCAR	CESM2-FV2	Danabasoglu (2019g, 2020c,d)
NCAR	CESM2-WACCM	Danabasoglu (2019c,e,f)
NCAR	CESM2-WACCM-FV2	Danabasoglu (2019d, 2020a,b)
	CMCC-CM2-SR5	
	CMCC-ESM2	
CMCC	CMCC-CM2-SR5	Lovato and Peano (2020a,b,c)
CMCC	CMCC-ESM2	Lovato et al. (2021a,b,c)
CCCma	CanESM5	Swart et al. (2019a,b,c)
EC-Earth-Consortium	EC-Earth3-AerChem	EC-Earth Consortium (2020a,b,c)
EC-Earth-Consortium	EC-Earth3-CC	EC-Earth Consortium (2020d,e, 2021)
EC-Earth-Consortium	EC-Earth3-Veg	EC-Earth Consortium (2019a,b,c)
NOAA-GFDL	GFDL-ESM4	Krasting et al. (2018a,b,c)
NASA-GISS	GISS-E2-1-G	NASA/GISS (2018a,b,c)
NASA-GISS	GISS-E2-2-G	NASA/GISS (2019a,b,c)
INM	INM-CM4-8	Volodin et al. (2019a,b,c)
IPSL	IPSL-CM6A-LR	Boucher et al. (2018a,b,c)
UA	MCM-UA-1-0	Stouffer (2019a,b,c)
MIROC	MIROC6	Tatebe and Watanabe (2018a,b,c)
HAMMOZ-Consortium	MPI-ESM-1-2-HAM	Neubauer et al. (2019a,b,c)
MPI-M, DWD, DKRZ	MPI-ESM1-2-HR	Jungclaus et al. (2019a,b,c)
MPI-M, AWI, DKRZ, DWD	MPI-ESM1-2-LR	Wieners et al. (2019a,b,c)
MRI	MRI-ESM2-0	Yukimoto et al. (2019a,b,c)
NCC	NorESM2-LM	Seland et al. (2019a,b,c)
NCC	NorESM2-MM	Bentsen et al. (2019a,b,c)
SNU	SAM0-UNICON	Park and Shin (2019a,b,c)
AS-RCEC	TaiESM1	Lee and Liang (2020a,b,c)

the mean state AMOC strength found in the 31 CMIP6 models in this study is consistent with previous studies using different model ensembles (Gregory et al. 2005; Jackson et al. 2020; Weaver et al. 2012; Winton et al. 2014).

How long does it take for the models to develop contrasting AMOC time evolution under CO_2 forcing? We find that the projected AMOC weakening differs a lot among models in the first decade of abrupt-4×CO_2 simulations, ranging from 0 to −10 Sv. About half of the spread at the end of the 150-yr simulations can already be observed in the first decade (Fig. 1b). Also, Welch's *t* test shows that the AMOC weakening between S10 and W10 is significantly different at 95% confidence level after year 4, echoing the fast-developing intermodel spread of AMOC weakening and its relation to mean state AMOC strength (Fig. S1 in the online supplemental material). In 1pctCO_2 simulations, the AMOC variations are weak in all models in the first 40 years and hence the intermodel spread is relatively small. This can be due to the comparable impacts from the forced and internal variability of the AMOC strength in the first 40 years. Starting around the year 40–50, the projected AMOC weakening exhibits quantitative differences, which can be well captured by the difference between S10 and W10 models. (Fig. 1c). Welch's *t* test shows that S10 and W10 models project significantly different AMOC changes at 95% confidence level at year 45, and a continuous and significant difference at 95% confidence level after year 52 (Fig. S1). In the following context, we will focus on the physical processes driving the diverse AMOC weakening in the first 10 years of abrupt-4×CO_2 simulations and years after the 40th in 1pctCO_2 simulations.

c. *Mean state climate in the North Atlantic*

The AMOC strength is tightly connected to the formation rate of deep water, which primarily occurs in the Labrador Sea and the Greenland–Iceland–Norwegian (GIN) Sea (Marshall and Schott 1999; Weaver et al. 1999). Here we report that the models with stronger mean state AMOC strength significantly correspond to weaker stratification in the upper (<500 m) Labrador Sea in the mean state climate (Figs. 2a,d,g). The models with stronger AMOC climatology bring warmer and saltier water from the subtropics into the cyclonic subpolar gyre in the upper ocean (Figs. 2b,c), corresponding to a warmer and saltier western subpolar gyre, especially in the Labrador Sea (Figs. 2e,f,h,i). The intermodel spread of salinity outweighs the spread of temperature in determining the upper Labrador Sea density among models in the mean state climate,

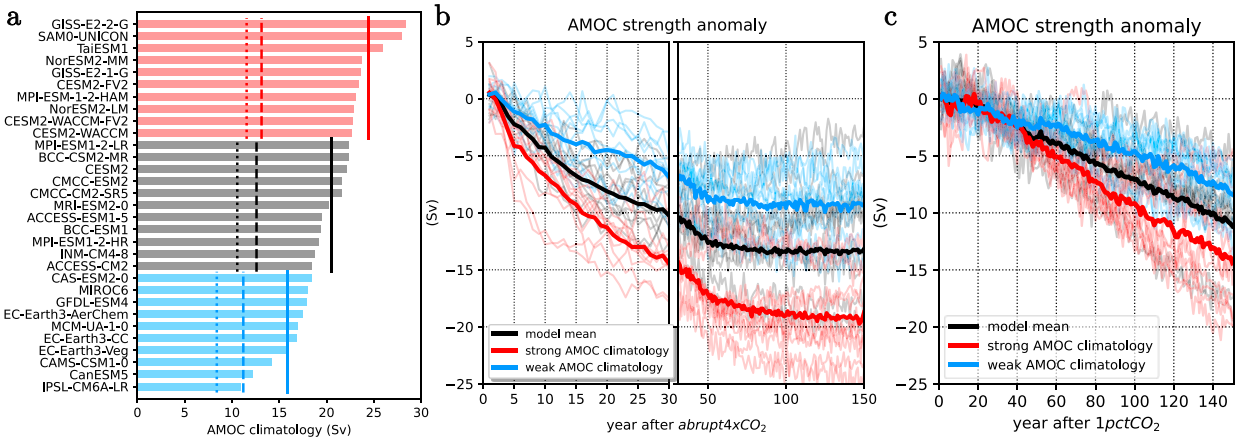

FIG. 1. (a) Climatological AMOC strength in 31 CMIP6 models. The strongest 10 models are colored in red (S10), and the weakest 10 models are in blue (W10). The remaining 11 models are in gray. Solid lines denote the ensemble mean of AMOC climatology in each group. Dashed lines denote the years 11–30 mean AMOC strength in abrupt-4×CO_2 simulations in each group. Dotted lines denote the years 131–150 mean AMOC strength in 1pctCO_2 simulations in each group. (b) AMOC weakening in abrupt-4×CO_2 simulations, sorted by the climatological AMOC strength. The black line denotes the 31-model mean. Red and blue lines denote the ensemble mean from S10 and W10 models, respectively. (c) As in (b), but for 1pctCO_2 simulations.

reflecting the large haline contraction coefficient at cold subpolar temperatures. In the GIN Sea, we find that the stratification in models is not related to the climatological AMOC strength. The intermodel correlation between the GIN Sea mean-state features (e.g., temperature, salinity, and density profiles) and the AMOC climatology is not significant, either (Figs. 2a–f). The result implies a tighter connection between the Labrador Sea and the AMOC strength across 35°N in the mean state climate in CMIP6 models.

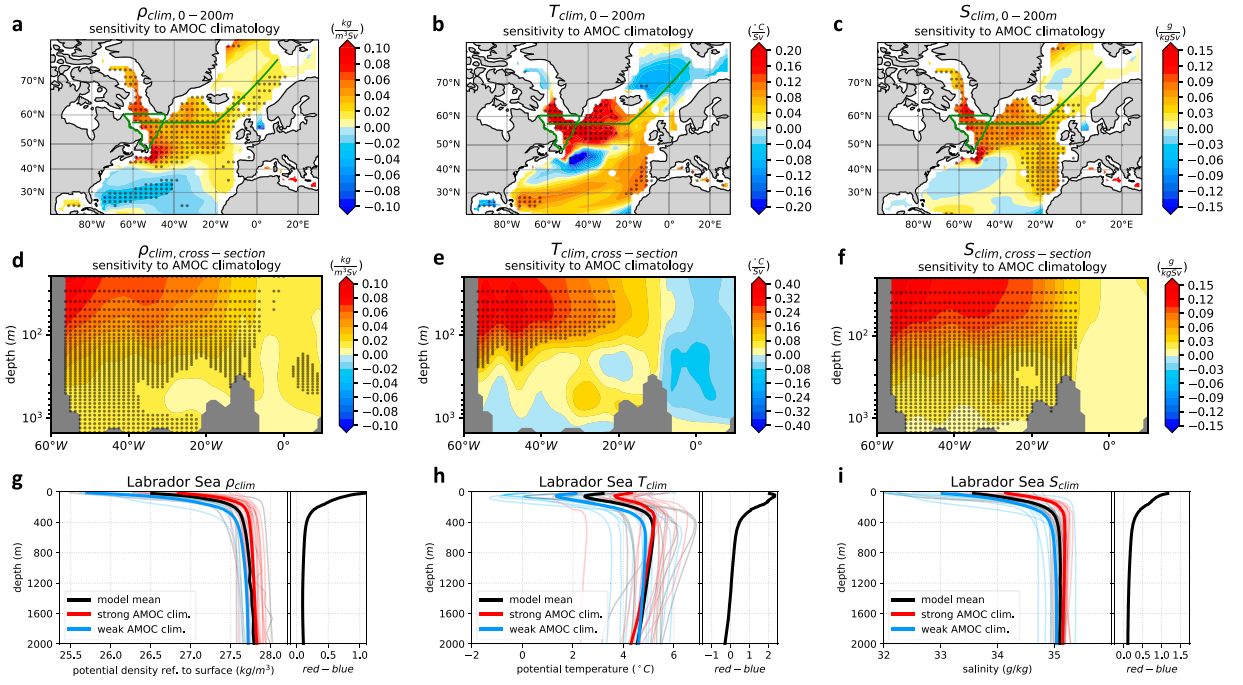

FIG. 2. Dependence of climatological potential density relative to the surface, potential temperature, and salinity on AMOC climatology. Regression slopes of climatological, 0–200-m averaged (a) potential density relative to the surface, (b) potential temperature, and (c) salinity against the AMOC climatology. Stippling denotes the significance at the 95% confidence level. (d)–(f) As in (a)–(c), but for the cross section from the Labrador Sea to GIN sea (track shown by the green line in the top row). Area-weighted average of (g) potential density relative to the surface (h) potential temperature and (i) salinity in the Labrador Sea (region shown by the green polygon between 50°–60°N and 40°–60°W in the top row). The black line denotes the 31-model mean, with red and blue lines denoting the ensemble mean from S10 and W10 models, respectively. Black lines in the right panels show the difference between red and blue lines (S10 − W10).

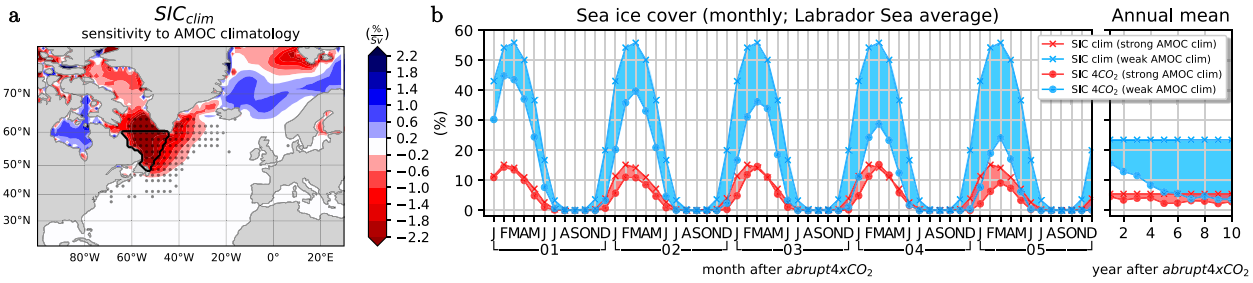

FIG. 3. (a) Regression slopes of climatological sea ice cover against AMOC climatology. Stippling denotes the significance at the 95% confidence level. (b) Monthly sea ice cover climatology (repeating annual cycle; lines with crosses) and in abrupt-4×CO_2 simulations (lines with dots). The red and blue lines denote the ensemble mean from S10 and W10 models, respectively. Note that the three models BCC-CSM2-MR, BCC-ESM1, and MCM-UA-1-0 are not included due to unavailable sea ice data.

3. Surface climate in the Labrador Sea

a. Sea ice

Consistent with a warmer and saltier upper ocean (Fig. 2), the sea ice extent is significantly less over the Labrador Sea in the mean state for the models with stronger AMOC climatology (Fig. 3a). The ensemble mean difference between S10 and W10 models reaches more than 30% (Fig. 3b). The sea ice loss under global warming would be insignificant if there is little sea ice to melt. Indeed, for those models with nearly ice-free Labrador Sea in the mean climate (i.e., strong AMOC climatology), there is barely any sea ice decline. In contrast, for the models with the abundant-ice-covered Labrador Sea in the mean state (i.e., weak AMOC climatology), the magnitudes of sea ice decline reach 10%–20% in the first 5 years of abrupt-4×CO_2 simulations. Note that the projected sea ice loss between S10 and W10 models already has contrasting magnitudes in the first month after CO_2 quadrupling, and this intermodel spread magnifies throughout the first 5 years until the sea ice cover in most of the models is all relatively small (about 5% in annual mean; Fig. 3b).

As for the seasonality of the sea ice decline, we report that the sea ice loss mostly happens in winter and spring. In summer and fall, the Labrador Sea is nearly ice-free in the mean climate, and thus sea ice responses under warming are negligible. To summarize, the models with stronger AMOC climatology, associated with less sea ice extent over the Labrador Sea in the mean climate of winter and spring, tend to project less sea ice decline over these two seasons under CO_2 forcing. The opposite is also true for the models with weaker AMOC climatology. The influences of the above intermodel spread of sea ice responses will be demonstrated later.

b. Surface energy budget

The sea ice decline could have multiple effects on the surface heat budget. First, the sea ice loss leads to weaker albedo that causes an increase in net incoming surface shortwave radiation (i.e., surface ice–albedo feedback). Second, the removal of the insulating sea ice creates an open water area for heat and moisture exchange between the atmosphere and the ocean (Serreze et al. 2009). As long as the ocean temperature is warmer than the atmosphere, with differences most pronounced in the wintertime, the climatologically upward turbulent heat fluxes would become stronger in response to sea ice decline.

Figure 4 shows that the intermodel spread of sea ice decline can be explained by the models with strong and weak AMOC climatology. Also, it indicates that the spread of sea ice responses has a greater impact on the spread of turbulent heat fluxes than shortwave radiation over the Labrador Sea, demonstrated as follows. For the models with weak AMOC climatology (i.e., strong sea ice decline), the surface downwelling net shortwave radiation does increase more than in other models, but the intermodel difference between S10 and W10 is small (peak value of 30 W m^{-2} in spring; Fig. 4c). At the same time, strong sea ice decline causes anomalous upward turbulent heat fluxes, which offset or even outweigh the anomalous downward heat fluxes from the warmer atmosphere under CO_2 forcing. Indeed, we do see a 30 W m^{-2} increase in upward turbulent heat fluxes in wintertime in the W10 models. On the other hand, in the S10 models that almost has no sea ice to melt, the upward turbulent heat fluxes weaken by more than 30 W m^{-2}. The intermodel difference thus reaches more than 60 W m^{-2} in winter between S10 and W10 models (Fig. 4b). Combined with the fact that the net longwave radiation anomalies are generally weak in all models (Fig. 4d), the spread of turbulent heat fluxes, associated with sea ice responses, is the dominant contributor to the spread of net surface flux responses to CO_2 forcing over the Labrador Sea (cf. Figs. 4a,b).

Since the AMOC is thought to be driven by deep water formation, in which the surface water releases heat and moisture to the atmosphere and forms the cold, deep water (Visbeck 2007), the above finding provides one possible physical interpretation of the dependence of the AMOC weakening on the AMOC climatology. For the models with stronger AMOC climatology and no sea ice decline, a larger decrease in upward turbulent heat fluxes leads to stronger AMOC weakening under CO_2 forcing. On the other hand, upward turbulent heat fluxes are barely suppressed (or even enhanced in winter) due to stronger sea ice decline in the models with weaker AMOC climatology, and thus the AMOC weakening is less significant. The above argument is consistent with the mechanism provided in Levermann et al. (2007). Also, it is consistent with the studies suggesting the dominant role of surface heat

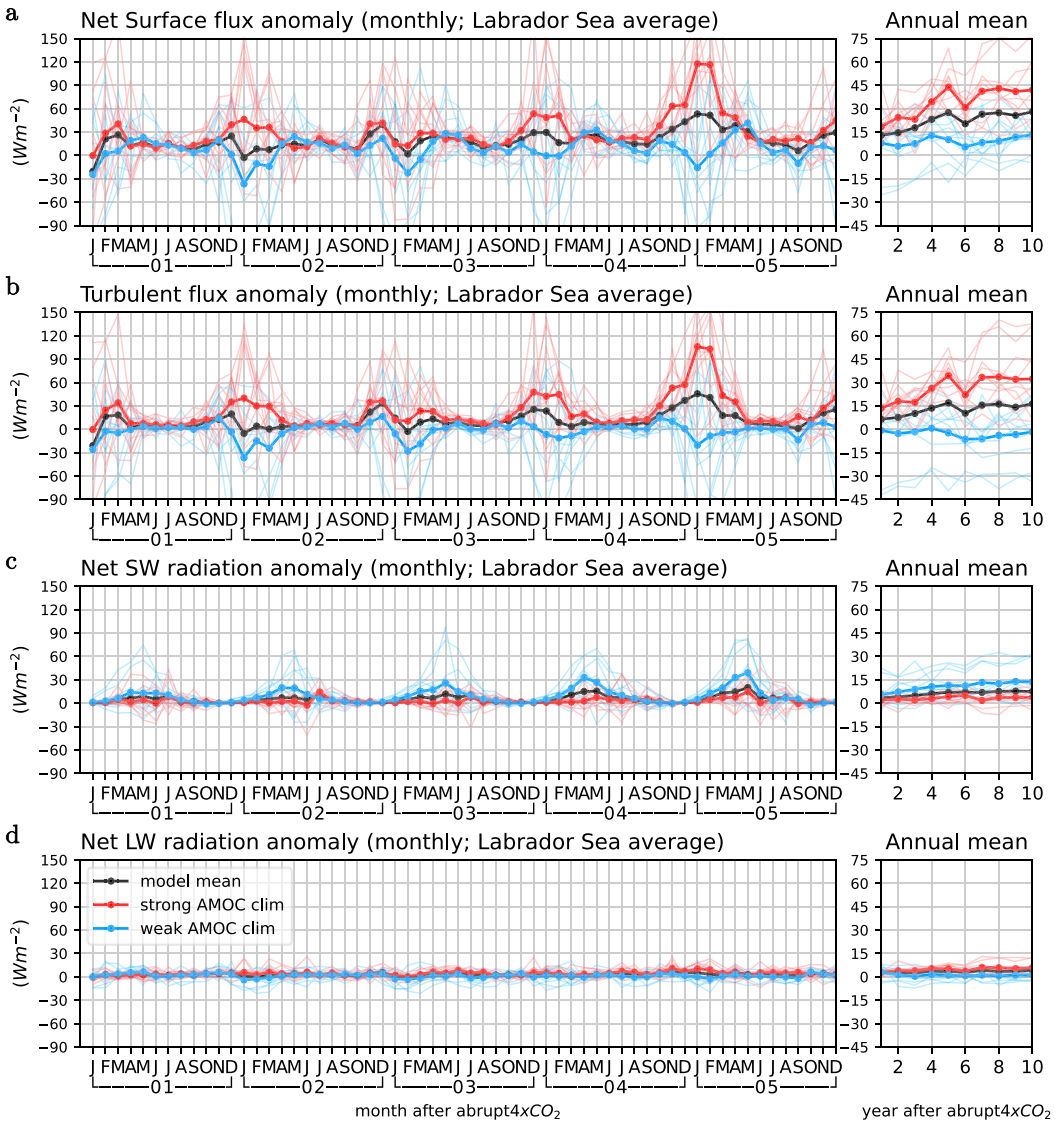

FIG. 4. Changes in (a) net surface flux, (b) the sum of the two turbulent heat fluxes (sensible heat flux and latent heat flux), (c) net shortwave radiation, and (d) net longwave radiation averaged over the Labrador Sea in abrupt-4×CO_2 simulations. Positive values indicate downward anomalies and negative values indicate upward anomalies. (left) The monthly mean responses in the first 5 years and (right) the annual-mean responses in the first 10 years. The red and blue lines denote the ensemble mean from S10 and W10 models, respectively. Note that the model MCM-UA-1-0 is not included due to unavailable data.

flux in weakening the AMOC rather than freshwater or momentum fluxes (Gregory et al. 2005, 2016).

However, how do the changes in the surface turbulent heat fluxes over the Labrador Sea affect the AMOC strength, defined at 35°N and 1000-m depth (generally the location of the strongest overturning)? What are the processes that translate the intermodel spread of forced responses in the subpolar region into the spread of subtropical AMOC weakening? Also, note that there is positive feedback involving the AMOC weakening and the anomalous turbulent heat fluxes that could amplify the correlation between the two features—the AMOC weakens in response to reduced upward turbulent heat fluxes, while the AMOC weakening causes the consequent cooling in the upper ocean, accounting for an even stronger reduction in the upwelling turbulent heat fluxes. In the next section, we will provide the time scales and the physical processes that are responsible for the intermodel spread of projected AMOC weakening, which can be further traced to the models' mean state climate.

4. Subsurface responses in the Labrador Sea

In this section, we show the processes and time scales by which the forced responses in the Labrador Sea lead to the AMOC weakening under CO_2 forcing, how those processes

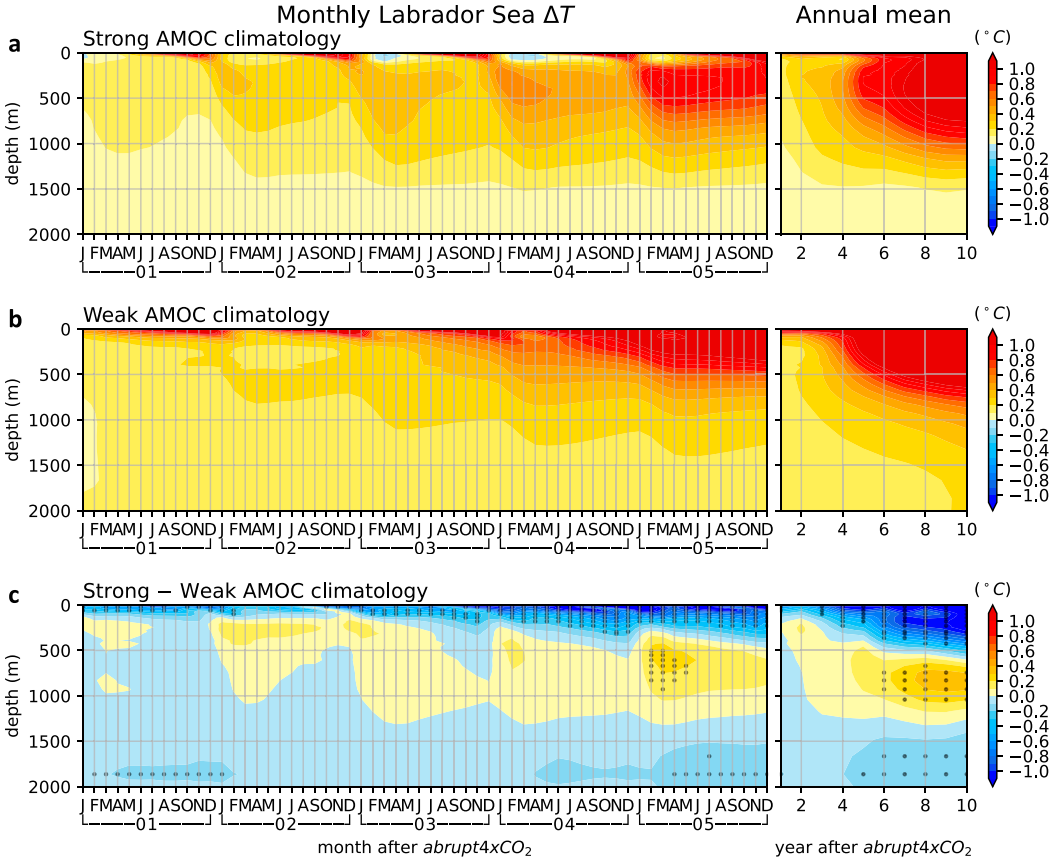

FIG. 5. Time evolution of the Labrador Sea averaged potential temperature responses in the models with (a) strong AMOC climatology (S10 models), (b) weak AMOC climatology (W10 models), and (c) their difference (S10 − W10) in abrupt-4×CO_2 simulations. Stippling denotes the significant difference between S10 and W10 at the 70% confidence level of the Welch's t test. (left) The monthly mean responses in the first 5 years and (right) the annual-mean responses in the first 10 years.

vary from model to model, and how they can be traced to the mean state climate in the Labrador Sea.

a. *Subsurface warming*

Figure 5 shows the vertical profile of temperature responses to CO_2 forcing in the Labrador Sea, with a focus on the seasonal structure over the first few years of adjustment. Generally, the warming is kept to the surface due to the climatologically stratified Labrador Sea in summer and fall. In winter and spring, the surface warming is mixed to the subsurface as the water is climatologically less stratified. This seasonality can be observed in all models regardless of their mean state AMOC strength. However, we also find that the warming responses are markedly different between models with strong and weak AMOC climatology, which are tightly connected to their mean state stratification. For the models with stronger AMOC climatology and the corresponding less stratified upper (<500 m) Labrador Sea (Fig. 2g), the mixing of the surface modified water to the subsurface is stronger. The less stratified Labrador Sea leads to enhanced warming in the subsurface and little warming (or even slight cooling) near the surface, especially during late winter to early spring (Fig. 5a). On the other hand, for the models with weaker mean state AMOC, the warming is more contained in the upper ocean (<500 m) due to the more stratified upper Labrador Sea in the mean state climate (Fig. 5b). The intermodel spread is shown when taking the difference between the models with strong and weak AMOC climatology, with the more pronounced subsurface warming difference occurring after around year 5. Those models with stronger mean state AMOC and less stratified upper Labrador Sea continuously bring surface warming down to the subsurface (Fig. 5c). The subsurface warming anomaly itself can also modify the stratification, as it would create a more stratified water column locally and keep the subsurface warming signal from penetrating all the way to the deep ocean. While most of the differences in the subsurface warming between S10 and W10 models are not significant ($0.2 < p < 0.3$), we note that the volume weighted, subsurface averaged warming over 500–1500 m is significantly stronger at 90% confidence ($p < 0.1$) in S10 models than in W10 models when excluding the model CAS-ESM2-0, especially in late winter to early spring around year 5 (Fig. S2). CAS-ESM2-0 is also the model with the strongest AMOC climatology of the W10

ensemble, thus excluding this model does not largely change our result linking the Labrador Sea subsurface warming to the AMOC climatology.

Multiple reasons could possibly account for the enhanced subsurface warming in the models with stronger mean state AMOC, including stronger downward surface heat flux anomalies, stronger vertical mixing of the heat, or stronger horizontal heat convergence at depth. Here we argue that stronger vertical mixing holds the key. For the models with stronger mean state AMOC, despite having stronger surface heat input under CO_2 forcing over the Labrador Sea (Fig. 4a), the warming responses over the Labrador Sea are not uniformly enhanced. Instead, the warming is only enhanced in the subsurface and largely reduced in the upper and deep Labrador Sea (Fig. 5c). The ocean heat content averaged over the Labrador Sea also agrees that less heat is kept in the Labrador Sea for the models with stronger surface heat input (not shown). In other words, the relatively enhanced subsurface warming in the S10 models is not due to the overall stronger warming by the surface heat input. It is, on the other hand, due to the heat distribution that favors the subsurface warming, especially in the late winter to early spring (Fig. 5c). As the vertical warming responses are shown to be dependent on the mean state AMOC, which corresponds to divergent upper-ocean stratification in the mean state climate (Fig. 2), we further deduce that the enhanced subsurface warming under CO_2 forcing in W10 models is likely to be caused by stronger vertical mixing in the upper Labrador Sea that is tightly linked to the mean state stratification.

b. *Attribution of the subsurface buoyancy flux*

As the modeled AMOC is close to the state of geostrophic balance (Levang and Schmitt 2020), the AMOC strength is largely determined by the density difference between the western and eastern margins of the Atlantic basin (Buckley and Marshall 2016; Buckley et al. 2012; Hirschi and Marotzke 2007). The enhanced subsurface warming in the Labrador Sea in S10 models (section 4a) could further weaken the AMOC across subtropical latitudes, following the southward transport of the relatively buoyant subsurface water by the deep western boundary current (DWBC). To test the hypothesis, we decompose the density responses to CO_2 forcing ($\Delta\rho$) into the contribution from temperature ($\Delta\rho_T$) and salinity ($\Delta\rho_S$), with potential nonlinearity noted as $\Delta\rho_{\text{nonlinear}}$. The reference state is the 150-yr-mean annual cycle of piControl simulation in each model (ρ_{piCtl}), which is also used to determine the monthly thermal expansion coefficient [$\alpha = (-1/\rho_{\text{piCtl}})(\partial\rho/\partial T)$; K^{-1}] and haline contraction coefficient [$\beta = (1/\rho_{\text{piCtl}})(\partial\rho/\partial S)$; kg g^{-1}].

$$\begin{cases} \Delta\rho = \rho_{\text{CO}_2} - \rho_{\text{piCtl}} \\ \Delta\rho_T = -\alpha\Delta T\rho_{\text{piCtl}} \\ \Delta\rho_S = \beta\Delta S\rho_{\text{piCtl}} \\ \Delta\rho_{\text{nonlinear}} = \Delta\rho - \Delta\rho_T - \Delta\rho_S \end{cases}. \tag{4.1}$$

Figure 6 suggests that the difference in the 500–1500 m, subsurface density anomaly between S10 and W10 models can be mostly traced to the temperature changes instead of the salinity component (cf. Fig. 6a with Figs. 6b,c). Consistent with the warming responses in the Labrador Sea, the surface buoyancy flux due to CO_2 forcing can penetrate to the subsurface Labrador Sea when the local mean state stratification is weak and is trapped in the upper ocean when the stratification is strong. The intermodel spread of salinity responses, on the other hand, is significantly dominant in modifying the density responses in the upper ocean shallower than 500 m (Fig. 6c). Also, the nonlinearity remains relatively small in this case (Fig. 6d). In summary, the relatively stronger decrease in the subsurface density decrease in S10 models can be mostly attributed to the relatively stronger warming in 500–1500 m. This relatively buoyant water in the subsurface Labrador Sea would act to weaken the AMOC in the subtropics through the southward transport by the DWBC (more discussion on the time scale in section 4d).

While the density responses in the Labrador Sea modify the AMOC strength as discussed above, one might think the changes in AMOC strength would also affect the water properties in the Labrador Sea. For example, the weaker northward heat and salt transport associated with the AMOC weakening would cause the upper water to be cooler and fresher in the North Atlantic. The positive salt–advection feedback amplifies both the salinity-related density decrease and the AMOC weakening, making it difficult to distinguish causality. However, the negative feedback between the AMOC weakening and the Labrador Sea subsurface warming excludes such ambiguity—the Labrador Sea subsurface warming would lead to the AMOC weakening, which reduces the Labrador Sea subsurface warming through a reduction in northward heat transport. As a result, we infer that the relatively enhanced subsurface warming (Fig. 5c) and the corresponding density decrease (Fig. 6b) are not the effects of stronger AMOC weakening. Instead, this model-dependent subsurface density response in the Labrador Sea acts as a precursor to AMOC weakening and an indicator of the weakening magnitude (see below). The role of subsurface density in changing the AMOC strength is consistent with previous studies highlighting the meridional connectivity between the subpolar and subtropical Atlantic (Ortega et al. 2021; Zhang 2010).

c. *1pctCO$_2$ simulations*

As mentioned in section 2b, the intermodel spread of the AMOC weakening is relatively small in the first 40 years of the 1pctCO_2 simulations due to comparable impacts from forced and internal variability of AMOC strength. Starting around year 40–50, magnitudes of the AMOC weakening differ among models, which can also be categorized into the group of strong and weak AMOC climatology (Fig. 1c; Fig. S1). Around the same time, the models with strong AMOC climatology tend to project enhanced warming in the subsurface Labrador Sea and slight cooling near the surface (<100 m; Fig. 7a). Warming is limited to the upper ocean for the models with weak AMOC climatology (Fig. 7b). When comparing the two groups of models, we see the slightly enhanced subsurface warming in 1000–1500 m and strongly reduced warming in the upper 500 m in the models with strong AMOC as opposed to weak AMOC strength. Consistent with abrupt-4×CO_2 simulations, the results can be explained by the less stratified mean-state Labrador Sea in the models with strong AMOC climatology, and vice versa. The

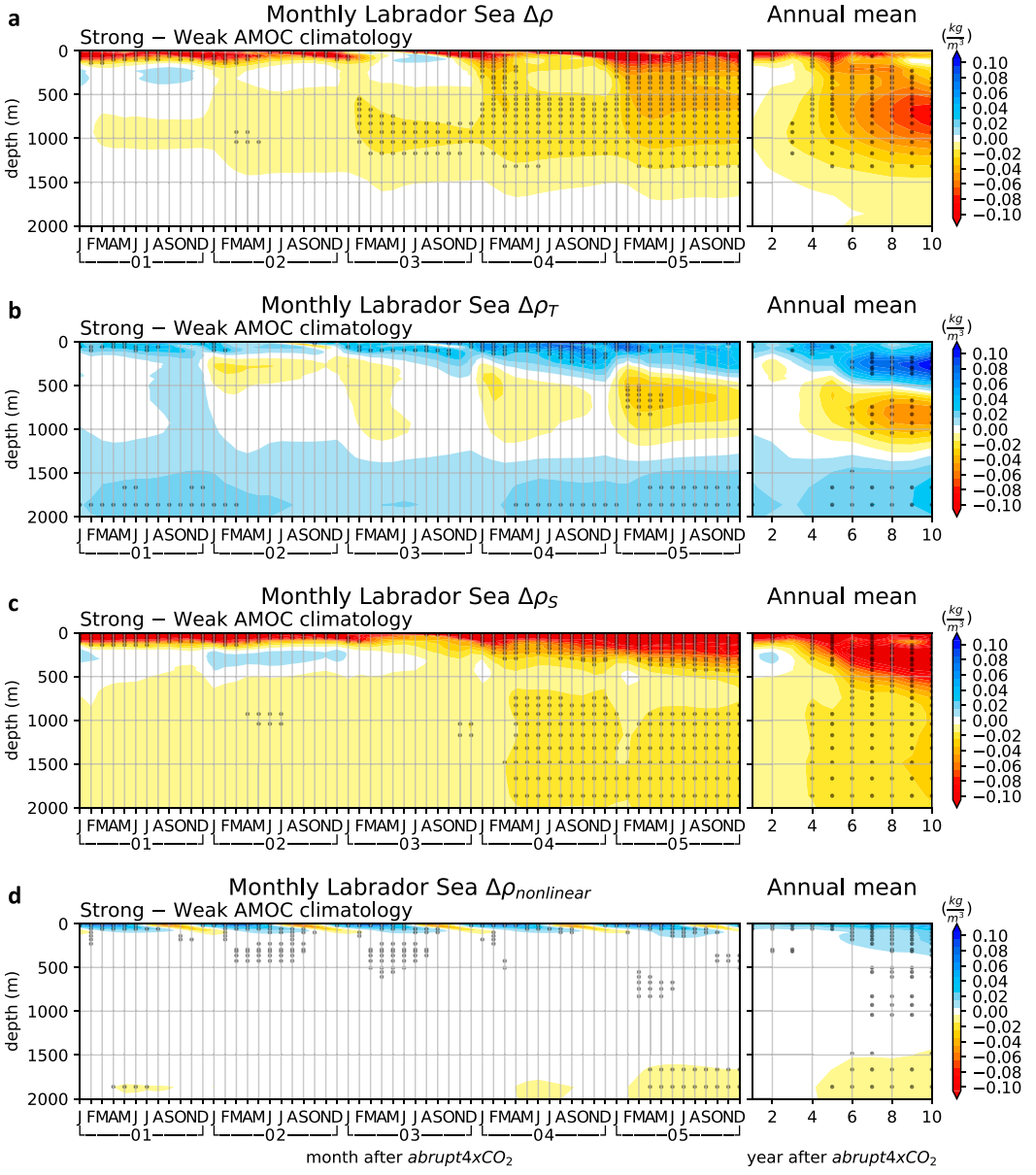

FIG. 6. Time evolution of the Labrador Sea averaged (a) potential density responses in abrupt-4×CO_2 simulations. Note that we only show the difference between S10 and W10 ensemble mean (S10 − W10). This intermodel difference in potential density responses can be further decomposed into (b) the contribution from potential temperature ($\Delta\rho_T$), (c) the contribution from salinity ($\Delta\rho_S$), and (d) the nonlinear term ($\Delta\rho_{\text{nonlinear}}$). Stippling denotes the significant difference between S10 and W10 at the 70% confidence level of the Welch's t test. (left) The monthly mean responses in the first 5 years and (right) the annual-mean responses in the first 10 years.

slow-building subsurface Labrador Sea warming in the models with stronger AMOC climatology at around year 40–50 would correspond to a larger decrease in density (not shown), implying a stronger AMOC weakening through communications by the DWBC.

d. Time series analysis

To provide further evidence of the causality between the decreasing subsurface (500–1500 m) density in the Labrador Sea and the AMOC weakening in CO_2-increase simulations in each CMIP6 model, we compare the year when each feature has its first significant decreasing (negative) linear trend at 99% confidence level ($p < 0.01$). Most CMIP6 models agree that the significant decrease in subsurface density leads the significant AMOC weakening by several years. There are 18 (out of 31) models that agree on the lead in abrupt-4×CO_2 simulations (Fig. 8a) and 27 (out of 31) models agree on the lead in 1pctCO_2 simulations (Fig. 8b).

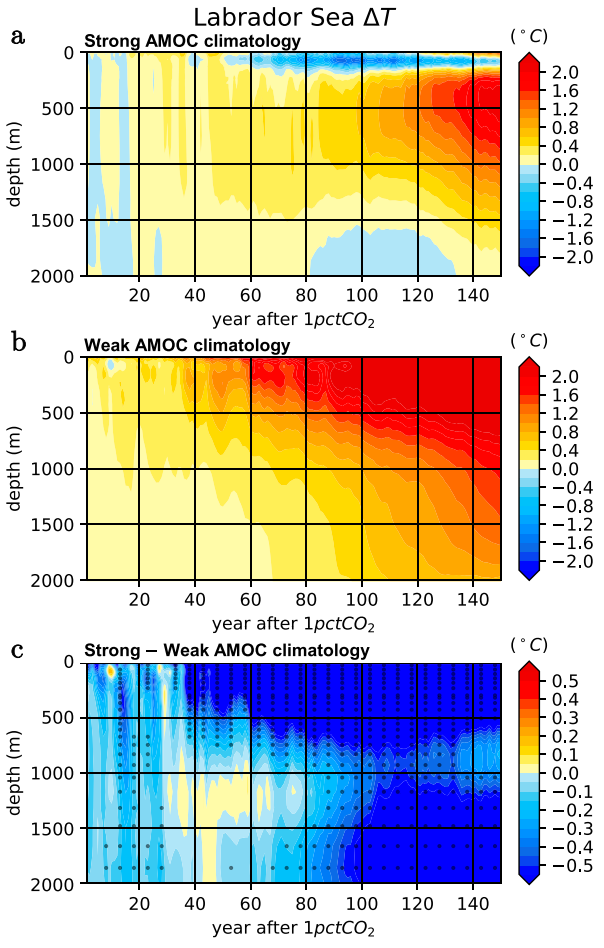

FIG. 7. Time evolution of the Labrador Sea averaged potential temperature responses in the models with (a) strong AMOC climatology (S10 models), (b) weak AMOC climatology (W10 models), and (c) their difference (S10 − W10) in 1pctCO_2 simulations. Stippling denotes the significant difference between S10 and W10 at the 70% confidence level of the Welch's *t* test.

In those models agreeing on the lead of the subsurface density (hereafter LEAD models), the lead time is generally 1–5 years, consistent with the advective time scale of the DWBC (Curry et al. 1998; Zhang 2010). In abrupt-4×CO_2 simulations, 16 out of 18 LEAD models agree on the leading time of 1–5 years. Only 2 models have slightly longer leading time of 6 and 7 years (Fig. 8a). In 1pctCO_2 simulations, however, only 12 out of 27 LEAD models have a time lead of 1–5 years, another 5 models lead by 6–10 years, another 6 models 11–20 years, and the other 4 models longer than 20 years (Fig. 8b).

Note that we should avoid overinterpreting the causal relationship based on the lead time discussed here. It is possible that the decreasing subsurface density and the AMOC weakening are not physically connected in the models with a long leading year (especially longer than 20 years). The earlier detection of the subsurface density trends can also be explained by its smaller interannual-to-decadal variability, comparing to the variability of AMOC strength.

Despite the caveats mentioned above, there is further evidence lending confidence to our physical interpretation of decreasing subsurface density in the Labrador Sea leading to the AMOC weakening trend. First, we find that the decadal variation of the Labrador Sea subsurface density leads the AMOC decadal variation by several years, simulated in piControl conditions in most of the CMIP6 models (Fig. S3). Second, the leading role and leading time of the Labrador Sea subsurface density is consistent with the previous studies using different model ensembles (Ortega et al. 2021; Roberts et al. 2013).

Figure 8 also shows that most of the LEAD models with a time lead of 1–5 years are the models with strong AMOC climatology (model on the *y* axis is sorted by its mean state AMOC strength). The result is consistent with the dependency of AMOC weakening on AMOC climatology (section 2b). For the models with weak AMOC climatology, the subsurface warming in the Labrador Sea is obscure (Fig. 5b for abrupt-4×CO_2 simulations and Fig. 7b for 1pctCO_2 simulations) and the AMOC weakening is also less significant (Figs. 1b,c). The lead–lag relationship is thus harder to detect because of the weak responses of the two features.

5. Idealized experiments

To address the mean state dependence of the AMOC weakening through modifying the vertical warming profile in the Labrador Sea (Fig. 5) and to understand the underlying physical processes, we restore temperature profiles in the Labrador Sea and find that the subsurface warming (500–1500 m) in the Labrador Sea drive the most pronounced AMOC weakening.

a. Model

The simulations are conducted in the National Center for Atmospheric Research Community Earth System Model version 1.2.1 (CESM1.2.1) in which only the ocean component—Parallel Ocean Program version 2 (POP2)—is active. It is an ocean model with the grid North Pole displaced into Greenland. In this study, we use the nominal 1° horizontal resolution version of the model. There are 60 vertical levels with thicknesses increasing from 10 m near the surface to about 250 m in the abyssal ocean. The atmosphere and the land runoff components read the boundary forcing data from a repeating annual cycle of the Coordinated Ocean Research Experiments version 2 (COREv2) dataset (Large and Yeager 2009). The sea ice component reads the data from a repeating annual cycle derived from the Special Sensor Microwave Imager (SSM/I) on board the Defense Meteorological Satellite Program (DMSP) satellites (Comiso 2000). Both datasets are representative of late-twentieth-century observations.

b. Experiment design

We first run a 300-yr control simulation, in which the AMOC strength and the deep ocean potential temperature have settled, and their trends remain weak in the last 30 years that we used. Six idealized experiments branched from the control simulation share the same model configuration, except that different vertical potential temperature anomalies are restored in the Labrador Sea. For each experiment, we run five ensemble members,

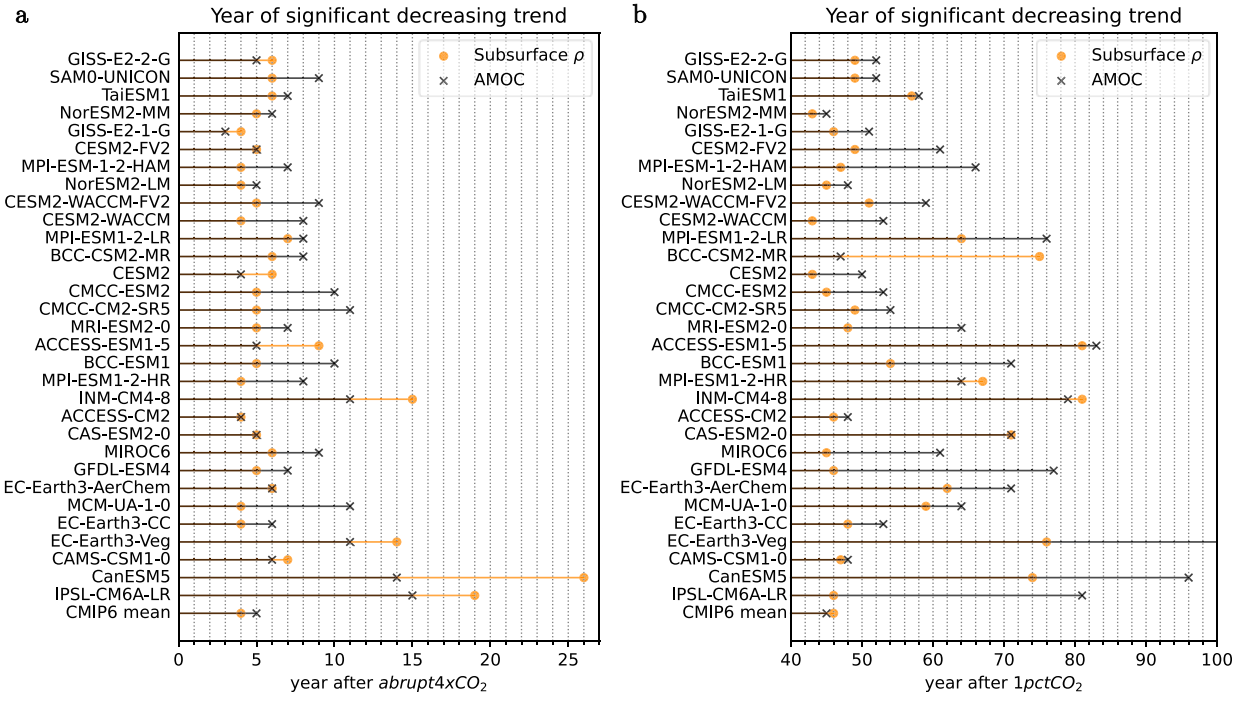

FIG. 8. The comparison between the year when the subsurface (500–1500 m) density in the Labrador Sea first has a significant decreasing trend at the 99% confidence level ($p < 0.01$; orange circles) and the AMOC strength first has a significant weakening trend at the 99% confidence level ($p < 0.01$; black crosses) in (a) abrupt-4×CO_2 simulations and (b) 1pctCO_2 simulations. The model on the y axis is sorted by its AMOC climatology. Note that in 1pctCO_2 simulations, the starting point for calculating the trend is the 40th year, consistent with Roberts and Palmer (2012).

with each being branched from the year 271, 276, 281, 286, and 291 of the control simulation.

In POP2, the ocean interior potential temperature T_{model} can be restored to T_{data} with a restoring time scale τ, shown as the following equation:

$$\frac{dT_{\text{model}}}{dt} = \frac{1}{\tau}(T_{\text{data}} - T_{\text{model}}). \tag{5.1}$$

We restore the potential temperature in the Labrador Sea by imposing an extra potential temperature forcing (T_{forcing}) onto the potential temperature in the control run (T_{control}), with a restoring time scale of 5 days. For each ensemble member, T_{control} is the monthly potential temperature taken from each branch year. Outside the Labrador Sea, we setup a 10-yr τ that is long enough for the potential temperature to nearly freely evolve within the first several years:

$$\begin{cases} T_{\text{data}} = T_{\text{control}} + T_{\text{forcing}}, & \text{in the Labrador Sea,} \\ T_{\text{data}} = T_{\text{control}}, & \text{otherwise} \end{cases}, \tag{5.2}$$

$$\begin{cases} \tau = 5\,\text{days}, & \text{in the Labrador Sea,} \\ \tau = 10\,\text{years}, & \text{otherwise} \end{cases}. \tag{5.3}$$

To elaborate on how the varying vertical warming profile in the Labrador Sea affects the AMOC weakening, we set the potential temperature forcing (T_{forcing}) as follows:

$$T_{\text{forcing}} = A\cos\left(\frac{z - z_c}{d}\pi\right), \quad z_c - \frac{d}{2} < z < z_c + \frac{d}{2}, \tag{5.4}$$

where z_c denotes the central depth of the forcing, d is the vertical span of the forcing, and A indicates the amplitude of the forcing. In all the six experiments, d is set to 500 m and A is set to 1°C. These two parameters are chosen based on the results from CMIP6 analysis, where the relatively enhanced subsurface warming spans 500 m and is on the order of 1°C (Fig. 5). The variable z_c, on the other hand, is set to six different depths separately at the six experiments—250, 500, 750, 1000, 1250, and 1500 m. Figure 9a shows the T_{forcing} that is separately applied to the six experiments.

c. Results

Figure 9b shows the AMOC strength in different experiments. Wherever the warming is imposed, the AMOC immediately has a weakening in the first 5 years. For the warming imposed in the subsurface Labrador Sea (z_c = 500, 750, 1000, 1250 m), the model projects stronger AMOC weakening, with the most pronounced weaking for z_c = 750 or 1000 m. In contrast, for the warming that is imposed in the upper (z_c = 250 m) or the deep Labrador Sea (z_c = 1500 m), the AMOC shows less significant weakening. The ensemble spread in the six experiments is small compared to the ensemble-mean responses (see thin lines in Fig. 9b), implying the weak

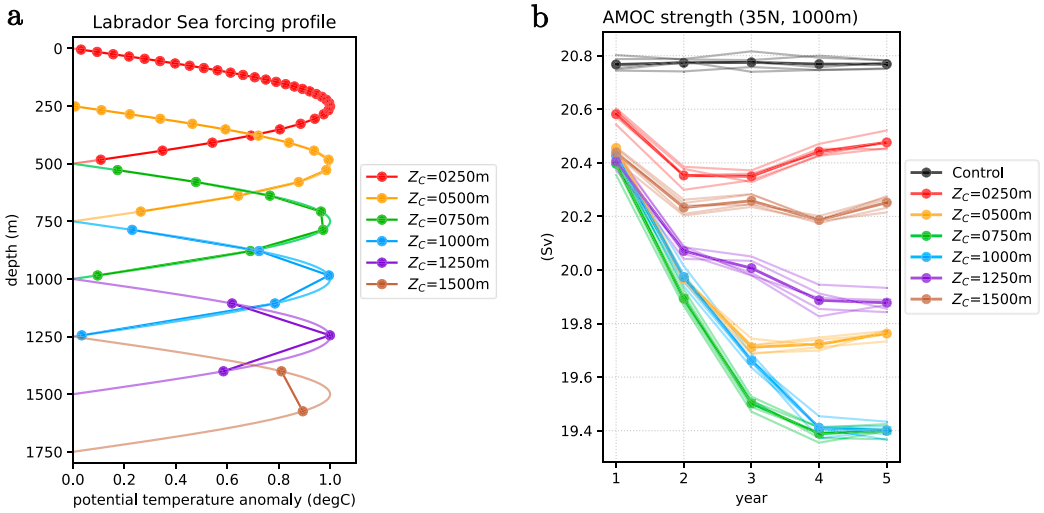

FIG. 9. (a) Potential temperature forcing (T_{forcing}) in the Labrador Sea in six experiments. (b) AMOC strength at 35°N and 1000-m depth. For each experiment, ensembles are shown as thin lines and the ensemble mean as a thick line. Dots in (a) indicate the vertical levels in the model used here.

interannual variability when the ocean is decoupled from the atmosphere.

Figure 10 shows the latitudinal structure of the AMOC weakening. In all simulations except for the upper ocean warming (z_c = 250 m), the AMOC weakens locally at the forcing latitudes (the Labrador Sea has a latitudinal span from 48° to 60°N). When the forcing is applied to the subsurface, the warming is carried by the DWBC, which leads to the density decrease along the west Atlantic, reduces the zonal density gradient (Fig. 11a), and drives the AMOC weakening, following the thermal wind balance (Buckley and Marshall 2016). We can clearly see the AMOC weakening in the subsurface warming experiments, starting from the subpolar region and propagating southward to the subtropics (Fig. 10). We can also see the warming along the west Atlantic coastline, which is responsible for the density decrease (Fig. 11b). On the other hand, the salinity responses partially offset the density decrease along the west Atlantic by temperature responses, acting to reduce the magnitudes of AMOC weakening in each simulation (Fig. 11c). The AMOC weakening stays locally when the warming is too deep for communication by the DWBC. In POP2, we find that this transition depth is around 1500 m (see z_c = 1500 m in Fig. 10).

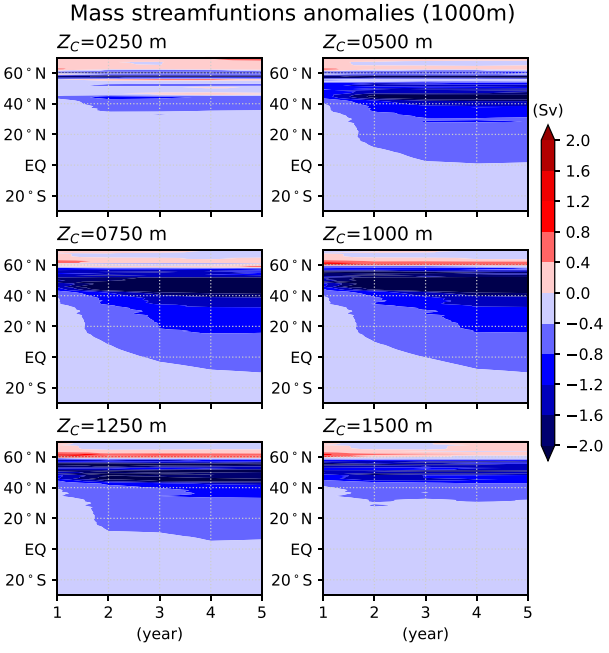

FIG. 10. Ensemble-mean anomalies of mass streamfunctions at 1000 m in each experiment.

The consistency shown between the idealized simulations and the CMIP6 analysis is at least twofold. First, simulations suggest that the imposed subsurface warming over 500–1500 m in Labrador Sea leads to stronger AMOC weakening (Fig. 9b). Across the CMIP6 models, those with enhanced subsurface warming at the depth of 500–1000 m correspond to stronger AMOC weakening in abrupt-4×CO_2 simulations (Fig. 5). Similar results are found in 1pctCO_2 simulations, but at the depth of 1000–1500 m (Fig. 7). Both idealized simulations and CMIP6 model spread analysis indicate that density changes at depths would lead to a stronger AMOC weakening. This result is also consistent with the previous research emphasizing the density variations at depths in driving the AMOC variations (Waldman et al. 2021). Second, idealized simulations support the proposed time scale in most CMIP6 models that the subsurface warming and density decrease lead the AMOC weakening by 1–5 years (Fig. 8), which is also consistent with the advective time scale of the DWBC (Curry et al. 1998; Zhang 2010).

Despite the consistency shown above, we note that the range of the AMOC responses to varying vertical forcing

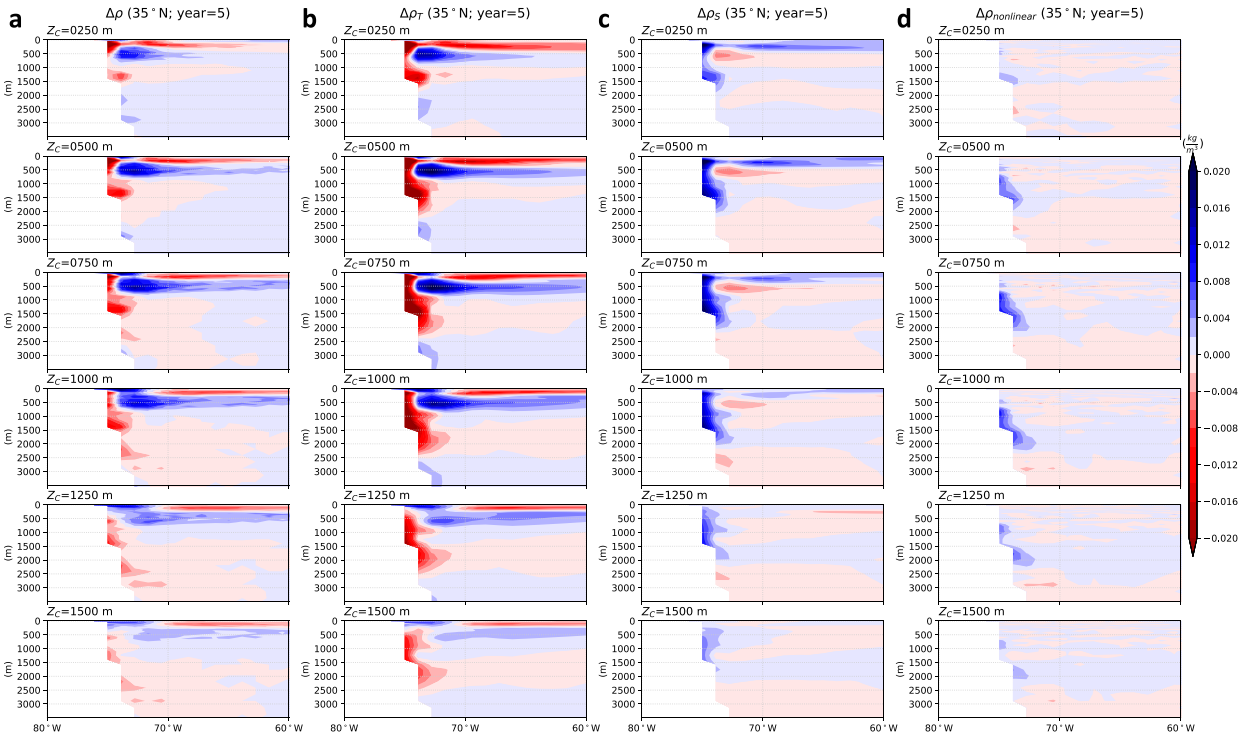

FIG. 11. Ensemble-mean responses of (a) potential density relative to the surface ($\Delta\rho$) along the cross section of 35°N at year 5 in each experiment. Contribution to $\Delta\rho$ (b) from potential temperature ($\Delta\rho_T$), (c) from salinity ($\Delta\rho_S$), and (d) the nonlinear term ($\Delta\rho_{\text{nonlinear}}$) from the decomposition.

profile is relatively small. The year-5 AMOC response to upper ocean warming (z_c = 250 m) is −0.3 Sv, and it is −1.4 Sv to subsurface ocean warming (z_c = 500, 750 m). The difference of 1.1 Sv is smaller than the CMIP6 intermodel spread of the AMOC weakening in most of the time (Figs. 1b,c). The small magnitudes could be attributed to multiple reasons. For example, the compensation between $\Delta\rho_T$ and $\Delta\rho_S$ described above (Fig. 11). In our ocean-only simulations without an active sea ice component, salinity changes due to sea ice variations are excluded, whereas the sea ice responses show large intermodel spread in CMIP6 models (Fig. 3) and could potentially have a strong influence on salinity responses. Also, the ocean-only simulations' lack of atmospheric coupling and positive feedbacks from the CMIP6 models, which might also explain the weaker AMOC decline in our simulations. In addition, oceanic warming is only imposed in the Labrador Sea to isolate its impact on the AMOC strength across 35°N, whereas the warming responses to CO_2 forcing in CMIP6 models are complex and the AMOC strength can be modified locally or remotely.

6. Conclusions and discussion

Due to the large uncertainty in the AMOC weakening and its corresponding broad climate impacts, it is important to narrow the intermodel spread of AMOC weakening under global warming. Here we find the dependence of AMOC weakening on the mean state AMOC strength in 31 CMIP6 models, consistent with previous studies (Gregory et al. 2005; Jackson et al. 2020; Weaver et al. 2012; Winton et al. 2014), implying that the mean state AMOC could act as an emergent constraint for the projected AMOC weakening. Also, we provide time scales and physical processes to explain the dependence of AMOC weakening on AMOC climatology, summarized in the schematic (Fig. 12).

For the models with strong mean state AMOC, the upper Labrador Sea is warmer, saltier, with less sea ice, and with stronger upward turbulent heat fluxes climatologically. The stratification over the upper ocean (<500 m) is weaker, thus the mixing is stronger (noted as a larger vortex sign in Fig. 12a; section 2) in the mean state climate. Within the first decade after CO_2 increase, the weak sea ice decline leads to little change in net shortwave radiation and stronger suppression of the upward turbulent heat fluxes (section 3). Also, the surface warming penetrates to the subsurface (>500 m) due to the stronger climatological mixing in the upper ocean (mixing noted as the larger vortex sign and temperature responses as ΔT in Fig. 12a; see also Fig. 5a), especially during late winter to early spring. The subsurface warming and the corresponding density decrease drive the AMOC weakening at a leading time scale of 1–5 years, consistent with the advective time scale of the DWBC (section 4). Idealized experiments support the driving role of subsurface warming in AMOC weakening. The subsurface warming occurring at 500–1500 m drives the most

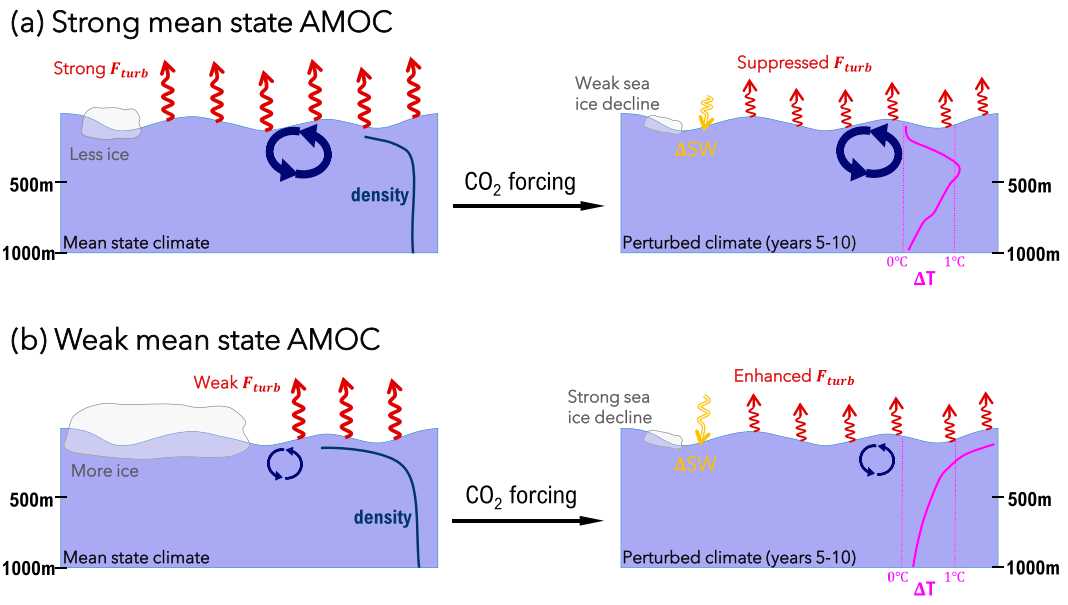

FIG. 12. The winter and spring schematic illustrating the contrasting mean state climate and projected climate years 5–10 after CO_2 increase in the Labrador Sea between the models with (a) strong and (b) weak mean state AMOC. The F_{turb} indicates the sum of the two turbulent heat fluxes (sensible heat flux and latent heat flux) in each climate state. Similarly, the blue vortex sign represents the strength of the upper-ocean mixing, and the blue line shows the vertical density profile in the Labrador Sea in each climate state. To better describe the CO_2-induced responses, Δ indicates the anomalous quantity under CO_2 forcing relative to the mean state climate. For example, ΔSW shows the net shortwave radiative responses and ΔT shows the potential temperature responses to CO_2 forcing.

pronounced AMOC weakening in a time scale of 1–5 years. For the simulations with significant AMOC weakening, the density is reduced through warming at 1000–2000 m along the subtropical western Atlantic, again highlighting the southward transport by the DWBC (section 5). Similarly (but with the opposite sign), for the models with weak mean state AMOC, the climatological stratification in the upper Labrador Sea is strong and the mixing is weak (noted as a smaller vortex sign in Fig. 12b), with extensive sea ice cover in the mean state. Under CO_2 forcing, the strong sea ice decline largely reduces the suppression of the turbulent heat loss by creating more open water area for heat and moisture exchanges. The turbulent heat loss even enhances in late winter to early spring in the first few years. Also, the warming in the Labrador Sea is trapped in the surface due to the strong mean state stratification in the first few years after CO_2 forcing (ΔT in Fig. 12b; see also Fig. 5b). The reduced subsurface warming corresponds to less pronounced subsurface density decrease in the Labrador Sea, and hence the AMOC weakening is also less significant in the models with weak AMOC climatology, in comparison with the strong AMOC climatology models. Here we argue the key physical factor governing the AMOC response to abrupt CO_2 forcing in the first few years is the climatological stratification in the Labrador Sea, which modifies the vertical warming profiles locally and in turn, affecting the magnitudes of the AMOC weakening.

Caution should be taken when interpreting the results. First, our proposed processes are used to interpret the CMIP6 intermodel spread of AMOC variations, thus the dominant uncertainty among models is shown and explained. For an individual model or multimodel mean, processes other than the role of the Labrador Sea subsurface warming might be more dominant in driving the AMOC weakening. Second, some studies with recent AMOC observation show that models have difficulty simulating the observed distribution of the deep water formation (Heuzé 2017; Jackson et al. 2022; Li et al. 2021; Liu et al. 2019; Lozier et al. 2019; Pickart and Spall 2007). For example, observation data from the Overturning in the Subpolar North Atlantic Program (OSNAP; Lozier et al. 2017) suggests little deep water forming in the Labrador Sea (Lozier et al. 2019). The relationship between interannual variations of the western boundary current and the overturning is weak in the observational records (Li et al. 2021). Compared with the observation, the Labrador Sea dense water formation in the models is usually biased strong (Jackson et al. 2020; Yeager et al. 2021), thus its link to the AMOC variations could also be overestimated. For now, the role of different deep convection sites in modifying the AMOC variations over multiple time scales is not fully understood, and the causes for the model biases on simulating the deep convection and dense water formation remain an open question.

One other potential caveat is the resolution of the models. Most of the CMIP6 models used in this study run the simulations with a horizontal ocean resolution of around 1°. Recent studies show that increasing horizontal ocean resolution in some models can reduce the model biases on the mean state AMOC, including its strength and depth (Menary et al. 2018) and the spatial structure of the horizontal flow (Yeager et al.

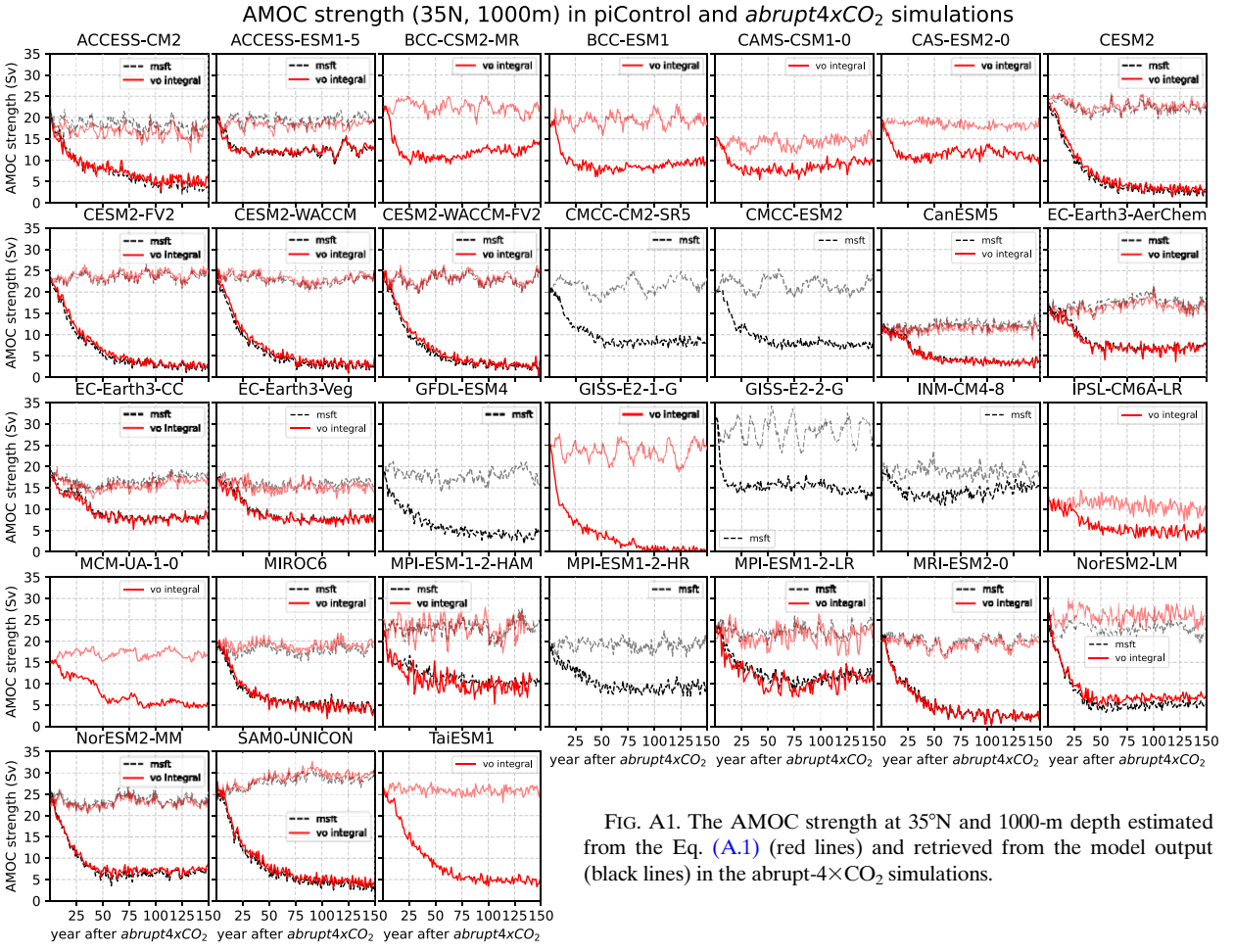

FIG. A1. The AMOC strength at 35°N and 1000-m depth estimated from the Eq. (A.1) (red lines) and retrieved from the model output (black lines) in the abrupt-4×CO_2 simulations.

2021). However, the results seem to be model dependent. Roberts et al. (2020) show that the sensitivity of the AMOC strength on ocean resolution can be positive or negative. Also, it is still under debate whether the increase in resolution is associated with stronger overturning in the east subpolar gyre or the west subpolar gyre (Jackson et al. 2020; Yeager et al. 2021). As our results highlight the role of mean state AMOC in determining the projected AMOC weakening, future work to constrain the present-day AMOC strength in models is needed for better AMOC projections.

Acknowledgments. We acknowledge the World Climate Research Programme, which, through its Working Group on Coupled Modelling, coordinated and promoted CMIP6. We thank the climate modeling groups (Table 1) for producing and making available their model output, the Earth System Grid Federation (ESGF) for archiving the data and providing access, and the multiple funding agencies who support CMIP6 and ESGF. Pangeo cloud-based datasets and several packages from Pangeo software ecosystem have been used to access or postprocess the model output (Abernathey et al. 2021). YJL and YTH were supported by the Ministry of Science and Technology of Taiwan (MOST 109-2917-I-002-005 and MOST 110-2628-M-002-002 for YJL and MOST 111-2628-M-002-003 for YTH). BEJR was supported by NSF Award ICER-2026863.

Data availability statement. The CMIP6 data used in this study can be accessed through the ESGF nodes (https://esgf-node.llnl.gov/search/cmip6/) and Pangeo cloud-based datasets. The code to setup the idealized simulations (section 5) and to reproduce the results of this study is available at https://github.com/yuanjenlin/Lin_etal_2022_JCLI.

APPENDIX

AMOC Strength Evaluation

To maximize the number of models in our analysis, we apply two methods to evaluate the AMOC strength; both show consistent results (Figs. A1 and A2). The first method is to simply use the model output of overturning mass streamfunctions (msftmz or msftyz). The second method is to integrate the meridional velocity (vo). The AMOC strength across a specific latitude (Ψ) can be estimated as follows:

$$\Psi(z) = \int_{xw}^{xe}\int_{-H}^{z} \mathrm{vo}(x, z)dz\,dx, \qquad (A.1)$$

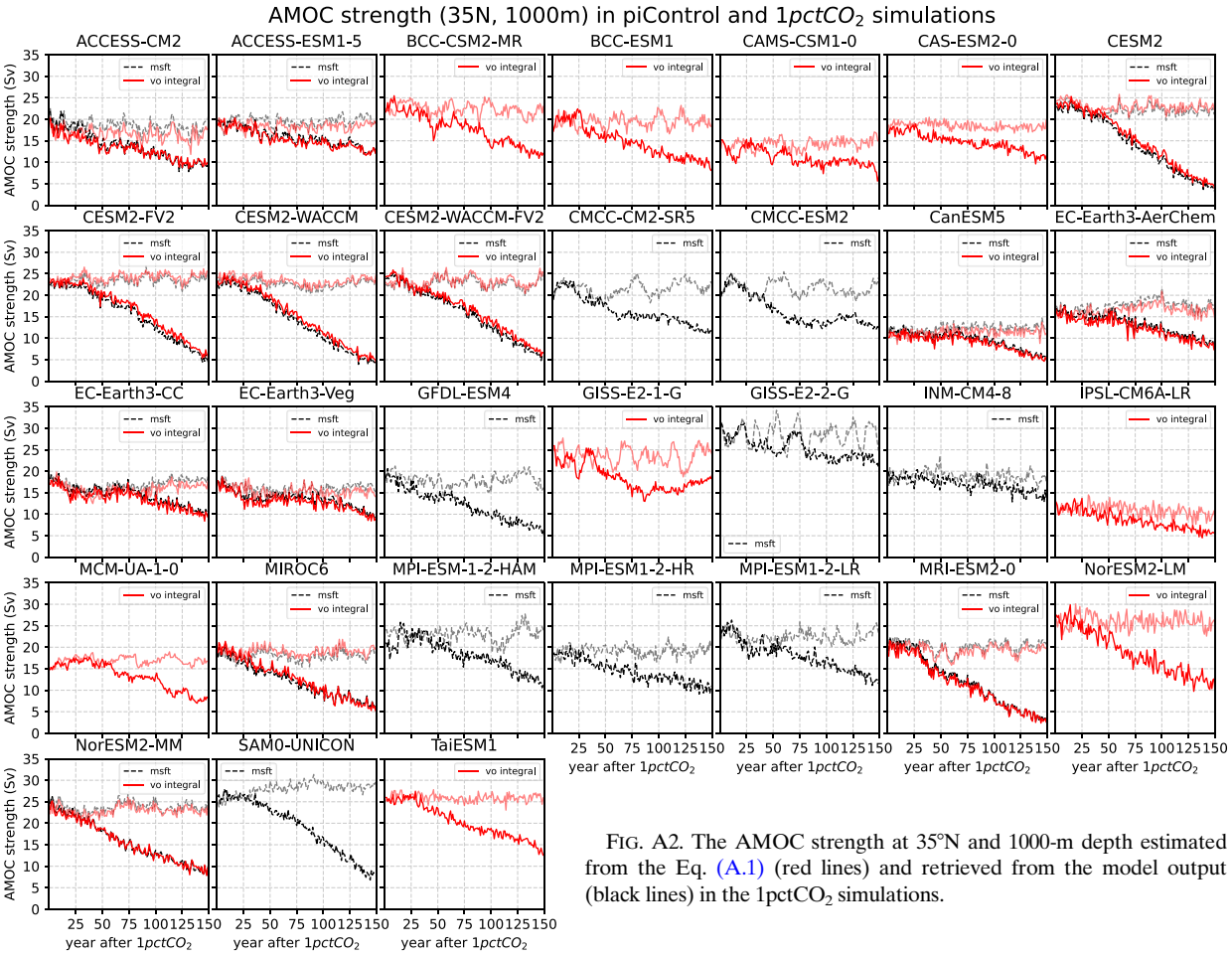

FIG. A2. The AMOC strength at 35°N and 1000-m depth estimated from the Eq. (A.1) (red lines) and retrieved from the model output (black lines) in the 1pctCO$_2$ simulations.

where the xw and xe are the western and eastern boundaries of the Atlantic, H is the ocean depth at each grid point, and z is the vertical coordinate.

In this study, the AMOC strength is calculated using the Eq. (A.1) if models only provide the meridional velocity. If models provide mass streamfunctions or provide both, we use the streamfunctions to determine the AMOC strength. In both abrupt-4×CO$_2$ (Fig. A1) and 1pctCO$_2$ (Fig. A2) simulations, the AMOC strength estimated from the Eq. (A.1) is consistent with the values of the model-generated streamfunctions.

REFERENCES

Abernathey, R. P., and Coauthors, 2021: Cloud-native repositories for big scientific data. *Comput. Sci. Eng.*, **23**, 26–35, https://doi.org/10.1109/MCSE.2021.3059437.

Bakker, P., and Coauthors, 2016: Fate of the Atlantic meridional overturning circulation: Strong decline under continued warming and Greenland melting. *Geophys. Res. Lett.*, **43**, 12 252–12 260, https://doi.org/10.1002/2016GL070457.

Bellomo, K., M. Angeloni, S. Corti, and J. von Hardenberg, 2021: Future climate change shaped by inter-model differences in Atlantic meridional overturning circulation response. *Nat. Commun.*, **12**, 3659, https://doi.org/10.1038/s41467-021-24015-w.

Bentsen, M., and Coauthors, 2019a: NCC NorESM2-MM model output prepared for CMIP6 CMIP 1pctCO2. Earth System Grid Federation, accessed 16 December 2021, https://doi.org/10.22033/ESGF/CMIP6.7806.

——, and Coauthors, 2019b: NCC NorESM2-MM model output prepared for CMIP6 CMIP abrupt-4xCO2. Earth System Grid Federation, accessed 16 December 2021, https://doi.org/10.22033/ESGF/CMIP6.7840.

——, and Coauthors, 2019c: NCC NorESM2-MM model output prepared for CMIP6 CMIP piControl. Earth System Grid Federation, accessed 16 December 2021, https://doi.org/10.22033/ESGF/CMIP6.8221.

Boucher, O., and Coauthors, 2018a: IPSL IPSL-CM6A-LR model output prepared for CMIP6 CMIP 1pctCO2. Earth System Grid Federation, accessed 16 December 2021, https://doi.org/10.22033/ESGF/CMIP6.5049.

——, and Coauthors, 2018b: IPSL IPSL-CM6A-LR model output prepared for CMIP6 CMIP abrupt-4xCO2. Earth System Grid Federation, accessed 16 December 2021, https://doi.org/10.22033/ESGF/CMIP6.5109.

——, and Coauthors, 2018c: IPSL IPSL-CM6A-LR model output prepared for CMIP6 CMIP piControl. Earth System Grid Federation, accessed 16 December 2021, https://doi.org/10.22033/ESGF/CMIP6.5251.

Buckley, M. W., and J. Marshall, 2016: Observations, inferences, and mechanisms of the Atlantic meridional overturning

circulation: A review. *Rev. Geophys.*, **54**, 5–63, https://doi.org/10.1002/2015RG000493.

——, D. Ferreira, J.-M. Campin, J. Marshall, and R. Tulloch, 2012: On the relationship between decadal buoyancy anomalies and variability of the Atlantic meridional overturning circulation. *J. Climate*, **25**, 8009–8030, https://doi.org/10.1175/JCLI-D-11-00505.1.

Chai, Z., 2020a: CAS CAS-ESM1.0 model output prepared for CMIP6 CMIP piControl. Earth System Grid Federation, accessed 16 December 2021, https://doi.org/10.22033/ESGF/CMIP6.3445.

——, 2020b: CAS CAS-ESM2.0 model output prepared for CMIP6 CMIP abrupt-4xCO2. Earth System Grid Federation, accessed 16 December 2021, https://doi.org/10.22033/ESGF/CMIP6.3174.

——, 2020c: CAS CAS-ESM2.0 model output prepared for CMIP6 CMIP 1pctCO2. Earth System Grid Federation, accessed 16 December 2021, https://doi.org/10.22033/ESGF/CMIP6.3052.

Chen, C., W. Liu, and G. Wang, 2019: Understanding the uncertainty in the 21st century dynamic sea level projections: The role of the AMOC. *Geophys. Res. Lett.*, **46**, 210–217, https://doi.org/10.1029/2018GL080676.

Comiso, J. C., 2000: Bootstrap sea ice concentrations from Nimbus-7 SMMR and DMSP SSM/I-SSMIS. Version 2, NASA National Snow and Ice Data Center Distributed Active Archive Center, accessed 16 December 2021, https://doi.org/10.5067/J6JQLS9EJ5HU.

Curry, R. G., M. S. McCartney, and T. M. Joyce, 1998: Oceanic transport of subpolar climate signals to mid-depth subtropical waters. *Nature*, **391**, 575–577, https://doi.org/10.1038/35356.

Danabasoglu, G., 2019a: NCAR CESM2 model output prepared for CMIP6 CMIP abrupt-4xCO2. Earth System Grid Federation, accessed 16 December 2021, https://doi.org/10.22033/ESGF/CMIP6.7519.

——, 2019b: NCAR CESM2 model output prepared for CMIP6 CMIP 1pctCO2. Earth System Grid Federation, accessed 16 December 2021, https://doi.org/10.22033/ESGF/CMIP6.7497.

——, 2019c: NCAR CESM2-WACCM model output prepared for CMIP6 CMIP 1pctCO2. Earth System Grid Federation, accessed 16 December 2021, https://doi.org/10.22033/ESGF/CMIP6.10028.

——, 2019d: NCAR CESM2-WACCM-FV2 model output prepared for CMIP6 CMIP piControl. Earth System Grid Federation, accessed 16 December 2021, https://doi.org/10.22033/ESGF/CMIP6.11302.

——, 2019e: NCAR CESM2-WACCM model output prepared for CMIP6 CMIP abrupt-4xCO2. Earth System Grid Federation, accessed 16 December 2021, https://doi.org/10.22033/ESGF/CMIP6.10039.

——, 2019f: NCAR CESM2-WACCM model output prepared for CMIP6 CMIP piControl. Earth System Grid Federation, accessed 16 December 2021, https://doi.org/10.22033/ESGF/CMIP6.10094.

——, 2019g: NCAR CESM2-FV2 model output prepared for CMIP6 CMIP piControl. Earth System Grid Federation, accessed 16 December 2021, https://doi.org/10.22033/ESGF/CMIP6.11301.

——, 2020a: NCAR CESM2-WACCM-FV2 model output prepared for CMIP6 CMIP 1pctCO2. Earth System Grid Federation, accessed 16 December 2021, https://doi.org/10.22033/ESGF/CMIP6.11284.

——, 2020b: NCAR CESM2-WACCM-FV2 model output prepared for CMIP6 CMIP abrupt-4xCO2. Earth System Grid Federation, accessed 16 December 2021, https://doi.org/10.22033/ESGF/CMIP6.11286.

——, 2020c: NCAR CESM2-FV2 model output prepared for CMIP6 CMIP abrupt-4xCO2. Earth System Grid Federation, accessed 16 December 2021, https://doi.org/10.22033/ESGF/CMIP6.11285.

——, 2020d: NCAR CESM2-FV2 model output prepared for CMIP6 CMIP 1pctCO2. Earth System Grid Federation, accessed 16 December 2021, https://doi.org/10.22033/ESGF/CMIP6.11283.

——, D. Lawrence, K. Lindsay, W. Lipscomb, and G. Strand, 2019: NCAR CESM2 model output prepared for CMIP6 CMIP piControl. Earth System Grid Federation, accessed 16 December 2021, https://doi.org/10.22033/ESGF/CMIP6.7733.

Delworth, T. L., and F. Zeng, 2012: Multicentennial variability of the Atlantic meridional overturning circulation and its climatic influence in a 4000 year simulation of the GFDL CM2.1 climate model. *Geophys. Res. Lett.*, **39**, L13702, https://doi.org/10.1029/2012GL052107.

——, and ——, 2016: The impact of the North Atlantic Oscillation on climate through its influence on the Atlantic meridional overturning circulation. *J. Climate*, **29**, 941–962, https://doi.org/10.1175/JCLI-D-15-0396.1.

Dima, M., D. R. Nichita, G. Lohmann, M. Ionita, and M. Voiculescu, 2021: Early-onset of Atlantic meridional overturning circulation weakening in response to atmospheric CO_2 concentration. *npj Climate Atmos. Sci.*, **4**, 27, https://doi.org/10.1038/s41612-021-00182-x.

Dix, M., and Coauthors, 2019a: CSIRO-ARCCSS ACCESS-CM2 model output prepared for CMIP6 CMIP 1pctCO2. Earth System Grid Federation, accessed 16 December 2021, https://doi.org/10.22033/ESGF/CMIP6.4230.

——, and Coauthors, 2019b: CSIRO-ARCCSS ACCESS-CM2 model output prepared for CMIP6 CMIP abrupt-4xCO2. Earth System Grid Federation, accessed 16 December 2021, https://doi.org/10.22033/ESGF/CMIP6.4237.

——, and Coauthors, 2019c: CSIRO-ARCCSS ACCESS-CM2 model output prepared for CMIP6 CMIP piControl. Earth System Grid Federation, accessed 16 December 2021, https://doi.org/10.22033/ESGF/CMIP6.4311.

Drijfhout, S. S., A. T. Blaker, S. A. Josey, A. J. G. Nurser, B. Sinha, and M. A. Balmaseda, 2014: Surface warming hiatus caused by increased heat uptake across multiple ocean basins. *Geophys. Res. Lett.*, **41**, 7868–7874, https://doi.org/10.1002/2014GL061456.

EC-Earth Consortium, 2019a: EC-Earth-Consortium EC-Earth3-Veg model output prepared for CMIP6 CMIP piControl. Earth System Grid Federation, accessed, https://doi.org/10.22033/ESGF/CMIP6.4848.

——, 2019b: EC-Earth-Consortium EC-Earth3-Veg model output prepared for CMIP6 CMIP 1pctCO2. Earth System Grid Federation, accessed 16 December 2021, https://doi.org/10.22033/ESGF/CMIP6.4507.

——, 2019c: EC-Earth-Consortium EC-Earth3-Veg model output prepared for CMIP6 CMIP abrupt-4xCO2. Earth System Grid Federation, accessed 16 December 2021, https://doi.org/10.22033/ESGF/CMIP6.4524.

——, 2020a: EC-Earth-Consortium EC-Earth3-AerChem model output prepared for CMIP6 CMIP piControl. Earth System Grid Federation, accessed 16 December 2021, https://doi.org/10.22033/ESGF/CMIP6.4843.

——, 2020b: EC-Earth-Consortium EC-Earth3-AerChem model output prepared for CMIP6 CMIP abrupt-4xCO2. Earth

System Grid Federation, accessed 16 December 2021, https://doi.org/10.22033/ESGF/CMIP6.4519.

——, 2020c: EC-Earth-Consortium EC-Earth3-AerChem model output prepared for CMIP6 CMIP 1pctCO2. Earth System Grid Federation, accessed 16 December 2021, https://doi.org/10.22033/ESGF/CMIP6.4502.

——, 2020d: EC-Earth-Consortium EC-Earth-3-CC model output prepared for CMIP6 CMIP 1pctCO2. Earth System Grid Federation, accessed 16 December 2021, https://doi.org/10.22033/ESGF/CMIP6.4503.

——, 2020e: EC-Earth-Consortium EC-Earth-3-CC model output prepared for CMIP6 CMIP abrupt-4xCO2. Earth System Grid Federation, accessed 16 December 2021, https://doi.org/10.22033/ESGF/CMIP6.4520.

——, 2021: EC-Earth-Consortium EC-Earth-3-CC model output prepared for CMIP6 CMIP piControl. Earth System Grid Federation, accessed 16 December 2021, https://doi.org/10.22033/ESGF/CMIP6.4844.

Eden, C., and T. Jung, 2001: North Atlantic interdecadal variability: Oceanic response to the North Atlantic Oscillation (1865–1997). *J. Climate*, **14**, 676–691, https://doi.org/10.1175/1520-0442(2001)014<0676:NAIVOR>2.0.CO;2.

——, and J. Willebrand, 2001: Mechanism of interannual to decadal variability of the North Atlantic circulation. *J. Climate*, **14**, 2266–2280, https://doi.org/10.1175/1520-0442(2001)014<2266:MOITDV>2.0.CO;2.

Gregory, J., and Coauthors, 2005: A model intercomparison of changes in the Atlantic thermohaline circulation in response to increasing atmospheric CO_2 concentration. *Geophys. Res. Lett.*, **32**, L12703, https://doi.org/10.1029/2005GL023209.

Gregory, J. M., and Coauthors, 2016: The Flux-Anomaly-Forced Model Intercomparison Project (FAFMIP) contribution to CMIP6: Investigation of sea-level and ocean climate change in response to CO_2 forcing. *Geosci. Model Dev.*, **9**, 3993–4017, https://doi.org/10.5194/gmd-9-3993-2016.

Haskins, R. K., K. I. C. Oliver, L. C. Jackson, R. A. Wood, and S. S. Drijfhout, 2020: Temperature domination of AMOC weakening due to freshwater hosing in two GCMs. *Climate Dyn.*, **54**, 273–286, https://doi.org/10.1007/s00382-019-04998-5.

Heuzé, C., 2017: North Atlantic deep water formation and AMOC in CMIP5 models. *Ocean Sci.*, **13**, 609–622, https://doi.org/10.5194/os-13-609-2017.

Hirschi, J., and J. Marotzke, 2007: Reconstructing the meridional overturning circulation from boundary densities and the zonal wind stress. *J. Phys. Oceanogr.*, **37**, 743–763, https://doi.org/10.1175/JPO3019.1.

Hirschi, J. J.-M., P. D. Killworth, and J. R. Blundell, 2007: Subannual, seasonal, and interannual variability of the north Atlantic meridional overturning circulation. *J. Phys. Oceanogr.*, **37**, 1246–1265, https://doi.org/10.1175/JPO3049.1.

Hu, A., G. A. Meehl, W. Han, and J. Yin, 2011: Effect of the potential melting of the Greenland ice sheet on the meridional overturning circulation and global climate in the future. *Deep-Sea Res. II*, **58**, 1914–1926, https://doi.org/10.1016/j.dsr2.2010.10.069.

——, L. Van Roekel, W. Weijer, O. A. Garuba, W. Cheng, and B. T. Nadiga, 2020: Role of AMOC in transient climate response to greenhouse gas forcing in two coupled models. *J. Climate*, **33**, 5845–5859, https://doi.org/10.1175/JCLI-D-19-1027.1.

IOC, SCOR, and IAPSO, 2010: The international thermodynamic equation of seawater – 2010: Calculation and use of thermodynamic properties. Intergovernmental Oceanographic Commission, Manuals and Guides 56, UNESCO, 196 pp., http://www.teos-10.org/pubs/TEOS-10_Manual.pdf.

IPCC, 2013: *Climate Change 2013: The Physical Science Basis*. Cambridge University Press, 1535 pp., https://doi.org/10.1017/CBO9781107415324.

——, 2021: *Climate Change 2021: The Physical Science Basis*. Cambridge University Press, 2391 pp., https://doi.org/10.1017/9781009157896.

Jackson, L. C., R. Kahana, T. Graham, M. A. Ringer, T. Woollings, J. V. Mecking, and R. A. Wood, 2015: Global and European climate impacts of a slowdown of the AMOC in a high resolution GCM. *Climate Dyn.*, **45**, 3299–3316, https://doi.org/10.1007/s00382-015-2540-2.

——, A. Peterson, C. D. Roberts, and R. A. Wood, 2016: Recent slowing of Atlantic overturning circulation as a recovery from earlier strengthening. *Nat. Geosci.*, **9**, 518–522, https://doi.org/10.1038/ngeo2715.

——, and Coauthors, 2020: Impact of ocean resolution and mean state on the rate of AMOC weakening. *Climate Dyn.*, **55**, 1711–1732, https://doi.org/10.1007/s00382-020-05345-9.

——, A. Biastoch, M. W. Buckley, D. G. Desbruyères, E. Frajka-Williams, B. Moat, and J. Robson, 2022: The evolution of the North Atlantic meridional overturning circulation since 1980. *Nat. Rev. Earth Environ.*, **3**, 241–254, https://doi.org/10.1038/s43017-022-00263-2.

Jungclaus, J., and Coauthors, 2019a: MPI-M MPI-ESM1.2-HR model output prepared for CMIP6 CMIP piControl. Earth System Grid Federation, accessed 16 December 2021, https://doi.org/10.22033/ESGF/CMIP6.6674.

——, and Coauthors, 2019b: MPI-M MPI-ESM1.2-HR model output prepared for CMIP6 CMIP abrupt-4xCO2. Earth System Grid Federation, accessed 16 December 2021, https://doi.org/10.22033/ESGF/CMIP6.6458.

——, and Coauthors, 2019c: MPI-M MPI-ESM1.2-HR model output prepared for CMIP6 CMIP 1pctCO2. Earth System Grid Federation, accessed 16 December 2021, https://doi.org/10.22033/ESGF/CMIP6.6434.

Knight, J. R., R. J. Allan, C. K. Folland, M. Vellinga, and M. E. Mann, 2005: A signature of persistent natural thermohaline circulation cycles in observed climate. *Geophys. Res. Lett.*, **32**, L20708, https://doi.org/10.1029/2005GL024233.

Köhl, A., 2005: Anomalies of meridional overturning: Mechanisms in the north Atlantic. *J. Phys. Oceanogr.*, **35**, 1455–1472, https://doi.org/10.1175/JPO2767.1.

Krasting, J. P., and Coauthors, 2018a: NOAA-GFDL GFDL-ESM4 model output prepared for CMIP6 CMIP 1pctCO2. Earth System Grid Federation, accessed 16 December 2021, https://doi.org/10.22033/ESGF/CMIP6.8473.

——, and Coauthors, 2018b: NOAA-GFDL GFDL-ESM4 model output prepared for CMIP6 CMIP piControl. Earth System Grid Federation, accessed 16 December 2021, https://doi.org/10.22033/ESGF/CMIP6.8669.

——, and Coauthors, 2018c: NOAA-GFDL GFDL-ESM4 model output prepared for CMIP6 CMIP abrupt-4xCO2. Earth System Grid Federation, accessed 16 December 2021, https://doi.org/10.22033/ESGF/CMIP6.8489.

Large, W. G., and S. G. Yeager, 2009: The global climatology of an interannually varying air–sea flux data set. *Climate Dyn.*, **33**, 341–364, https://doi.org/10.1007/s00382-008-0441-3.

Lee, W.-L., and H.-C. Liang, 2020a: AS-RCEC TaiESM1.0 model output prepared for CMIP6 CMIP 1pctCO2. Earth System Grid Federation, accessed 16 December 2021, https://doi.org/10.22033/ESGF/CMIP6.9702.

——, and ——, 2020b: AS-RCEC TaiESM1.0 model output prepared for CMIP6 CMIP piControl. Earth System Grid Federation, accessed 16 December 2021, https://doi.org/10.22033/ESGF/CMIP6.9798.

——, and ——, 2020c: AS-RCEC TaiESM1.0 model output prepared for CMIP6 CMIP abrupt-4xCO2. Earth System Grid Federation, accessed 16 December 2021, https://doi.org/10.22033/ESGF/CMIP6.9709.

Levang, S. J., and R. W. Schmitt, 2020: What causes the AMOC to weaken in CMIP5? *J. Climate*, **33**, 1535–1545, https://doi.org/10.1175/JCLI-D-19-0547.1.

Levermann, A., J. Mignot, S. Nawrath, and S. Rahmstorf, 2007: The role of northern sea ice cover for the weakening of the thermohaline circulation under global warming. *J. Climate*, **20**, 4160–4171, https://doi.org/10.1175/JCLI4232.1.

Li, F., and Coauthors, 2021: Subpolar North Atlantic western boundary density anomalies and the meridional overturning circulation. *Nat. Commun.*, **12**, 3002, https://doi.org/10.1038/s41467-021-23350-2.

Little, C. M., A. Hu, C. W. Hughes, G. D. Mccarthy, C. G. Piecuch, R. M. Ponte, and M. D. Thomas, 2019: The relationship between U.S. East Coast sea level and the Atlantic meridional overturning circulation: A review. *J. Geophys. Res. Oceans*, **124**, 6435–6458, https://doi.org/10.1029/2019JC015152.

Liu, W., and A. V. Fedorov, 2019: Global impacts of arctic sea ice loss mediated by the Atlantic meridional overturning circulation. *Geophys. Res. Lett.*, **46**, 944–952, https://doi.org/10.1029/2018GL080602.

——, A. Fedorov, and F. Sévellec, 2019: The mechanisms of the Atlantic meridional overturning circulation slowdown induced by Arctic sea ice decline. *J. Climate*, **32**, 977–996, https://doi.org/10.1175/JCLI-D-18-0231.1.

——, A. V. Fedorov, S.-P. Xie, and S. Hu, 2020: Climate impacts of a weakened Atlantic meridional overturning circulation in a warming climate. *Sci. Adv.*, **6**, eaaz4876, https://doi.org/10.1126/sciadv.aaz4876.

Lohmann, K., H. Drange, and M. Bentsen, 2009: Response of the North Atlantic subpolar gyre to persistent North Atlantic oscillation like forcing. *Climate Dyn.*, **32**, 273–285, https://doi.org/10.1007/s00382-008-0467-6.

Lovato, T., and D. Peano, 2020a: CMCC CMCC-CM2-SR5 model output prepared for CMIP6 CMIP abrupt-4xCO2. Earth System Grid Federation, accessed 16 December 2021, https://doi.org/10.22033/ESGF/CMIP6.3731.

——, and ——, 2020b: CMCC CMCC-CM2-SR5 model output prepared for CMIP6 CMIP piControl. Earth System Grid Federation, accessed 16 December 2021, https://doi.org/10.22033/ESGF/CMIP6.3874.

——, and ——, 2020c: CMCC CMCC-CM2-SR5 model output prepared for CMIP6 CMIP 1pctCO2. Earth System Grid Federation, accessed 16 December 2021, https://doi.org/10.22033/ESGF/CMIP6.3721.

——, ——, and M. Butenschön, 2021a: CMCC CMCC-ESM2 model output prepared for CMIP6 CMIP abrupt-4xCO2. Earth System Grid Federation, accessed 16 December 2021, https://doi.org/10.22033/ESGF/CMIP6.13174.

——, ——, and ——, 2021b: CMCC CMCC-ESM2 model output prepared for CMIP6 CMIP piControl. Earth System Grid Federation, accessed 16 December 2021, https://doi.org/10.22033/ESGF/CMIP6.13241.

——, ——, and ——, 2021c: CMCC CMCC-ESM2 model output prepared for CMIP6 CMIP 1pctCO2. Earth System Grid Federation, accessed 16 December 2021, https://doi.org/10.22033/ESGF/CMIP6.13169.

Lozier, M. S., and Coauthors, 2017: Overturning in the subpolar North Atlantic program: A new international ocean observing system. *Bull. Amer. Meteor. Soc.*, **98**, 737–752, https://doi.org/10.1175/BAMS-D-16-0057.1.

——, and Coauthors, 2019: A sea change in our view of overturning in the subpolar North Atlantic. *Science*, **363**, 516–521, https://doi.org/10.1126/science.aau6592.

Mahajan, S., R. Zhang, and T. L. Delworth, 2011: Impact of the Atlantic meridional overturning circulation (AMOC) on Arctic surface air temperature and sea ice variability. *J. Climate*, **24**, 6573–6581, https://doi.org/10.1175/2011JCLI4002.1.

Marshall, J., and F. Schott, 1999: Open-ocean convection: Observations, theory, and models. *Rev. Geophys.*, **37**, 1–64, https://doi.org/10.1029/98RG02739.

Menary, M. B., W. Park, K. Lohmann, M. Vellinga, M. D. Palmer, M. Latif, and J. H. Jungclaus, 2012: A multimodel comparison of centennial Atlantic meridional overturning circulation variability. *Climate Dyn.*, **38**, 2377–2388, https://doi.org/10.1007/s00382-011-1172-4.

——, and Coauthors, 2018: Preindustrial control simulations with HadGEM3-GC3.1 for CMIP6. *J. Adv. Model. Earth Syst.*, **10**, 3049–3075, https://doi.org/10.1029/2018MS001495.

——, and Coauthors, 2020: Aerosol-forced AMOC changes in CMIP6 historical simulations. *Geophys. Res. Lett.*, **47**, e2020GL088166, https://doi.org/10.1029/2020GL088166.

Moreno-Chamarro, E., J. Marshall, and T. Delworth, 2019: Linking ITCZ migrations to AMOC and North Atlantic/Pacific SST decadal variability. *J. Climate*, **33**, 893–905, https://doi.org/10.1175/JCLI-D-19-0258.1.

Muir, L., and A. Fedorov, 2015: How the AMOC affects ocean temperatures on decadal to centennial timescales: The North Atlantic versus an interhemispheric seesaw. *Climate Dyn.*, **45**, 151–160, https://doi.org/10.1007/s00382-014-2443-7.

NASA/GISS, 2018a: NASA-GISS GISS-E2.1G model output prepared for CMIP6 CMIP 1pctCO2. Earth System Grid Federation, accessed 16 December 2021, https://doi.org/10.22033/ESGF/CMIP6.6950.

——, 2018b: NASA-GISS GISS-E2.1G model output prepared for CMIP6 CMIP abrupt-4xCO2. Earth System Grid Federation, accessed 16 December 2021, https://doi.org/10.22033/ESGF/CMIP6.6976.

——, 2018c: NASA-GISS GISS-E2.1G model output prepared for CMIP6 CMIP piControl. Earth System Grid Federation, accessed 16 December 2021, https://doi.org/10.22033/ESGF/CMIP6.7380.

——, 2019a: NASA-GISS GISS-E2-2-G model output prepared for CMIP6 CMIP abrupt-4xCO2. Earth System Grid Federation, accessed 16 December 2021, https://doi.org/10.22033/ESGF/CMIP6.6978.

——, 2019b: NASA-GISS GISS-E2-2-G model output prepared for CMIP6 CMIP 1pctCO2. Earth System Grid Federation, accessed 16 December 2021, https://doi.org/10.22033/ESGF/CMIP6.6952.

——, 2019c: NASA-GISS GISS-E2-2-G model output prepared for CMIP6 CMIP piControl. Earth System Grid Federation, accessed 16 December 2021, https://doi.org/10.22033/ESGF/CMIP6.7382.

Neubauer, D., and Coauthors, 2019a: HAMMOZ-Consortium MPI-ESM1.2-HAM model output prepared for CMIP6 CMIP piControl. Earth System Grid Federation, accessed 16 December 2021, https://doi.org/10.22033/ESGF/CMIP6.5037.

——, and Coauthors, 2019b: HAMMOZ-Consortium MPI-ESM1.2-HAM model output prepared for CMIP6 CMIP abrupt-4xCO2. Earth System Grid Federation, accessed 16 December 2021, https://doi.org/10.22033/ESGF/CMIP6.5000.

——, and Coauthors, 2019c: HAMMOZ-Consortium MPI-ESM1.2-HAM model output prepared for CMIP6 CMIP 1pctCO2. Earth System Grid Federation, accessed 16 December 2021, https://doi.org/10.22033/ESGF/CMIP6.4999.

Ortega, P., and Coauthors, 2021: Labrador Sea subsurface density as a precursor of multidecadal variability in the North Atlantic: A multi-model study. *Earth Syst. Dyn.*, **12**, 419–438, https://doi.org/10.5194/esd-12-419-2021.

Park, S., and J. Shin, 2019a: SNU SAM0-UNICON model output prepared for CMIP6 CMIP piControl. Earth System Grid Federation, accessed 16 December 2021, https://doi.org/10.22033/ESGF/CMIP6.7791.

——, and ——, 2019b: SNU SAM0-UNICON model output prepared for CMIP6 CMIP abrupt-4xCO2. Earth System Grid Federation, accessed 16 December 2021, https://doi.org/10.22033/ESGF/CMIP6.7783.

——, and ——, 2019c: SNU SAM0-UNICON model output prepared for CMIP6 CMIP 1pctCO2. Earth System Grid Federation, accessed 16 December 2021, https://doi.org/10.22033/ESGF/CMIP6.7782.

Parsons, L. A., J. Yin, J. T. Overpeck, R. J. Stouffer, and S. Malyshev, 2014: Influence of the Atlantic meridional overturning circulation on the monsoon rainfall and carbon balance of the American tropics. *Geophys. Res. Lett.*, **41**, 146–151, https://doi.org/10.1002/2013GL058454.

Pickart, R. S., and M. A. Spall, 2007: Impact of Labrador Sea convection on the north Atlantic meridional overturning circulation. *J. Phys. Oceanogr.*, **37**, 2207–2227, https://doi.org/10.1175/JPO3178.1.

Reintges, A., T. Martin, M. Latif, and N. S. Keenlyside, 2017: Uncertainty in twenty-first century projections of the Atlantic meridional overturning circulation in CMIP3 and CMIP5 models. *Climate Dyn.*, **49**, 1495–1511, https://doi.org/10.1007/s00382-016-3180-x.

Roberts, C. D., and M. D. Palmer, 2012: Detectability of changes to the Atlantic meridional overturning circulation in the Hadley Centre climate models. *Climate Dyn.*, **39**, 2533–2546, https://doi.org/10.1007/s00382-012-1306-3.

——, F. K. Garry, and L. C. Jackson, 2013: A multimodel study of sea surface temperature and subsurface density fingerprints of the Atlantic meridional overturning circulation. *J. Climate*, **26**, 9155–9174, https://doi.org/10.1175/JCLI-D-12-00762.1.

Roberts, M. J., and Coauthors, 2020: Sensitivity of the Atlantic meridional overturning circulation to model resolution in CMIP6 HighResMIP simulations and implications for future changes. *J. Adv. Model. Earth Syst.*, **12**, e2019MS002014, https://doi.org/10.1029/2019MS002014.

Rong, X., 2019a: CAMS CAMS_CSM1.0 model output prepared for CMIP6 CMIP abrupt-4xCO2. Earth System Grid Federation, accessed 16 December 2021, https://doi.org/10.22033/ESGF/CMIP6.9708.

——, 2019b: CAMS CAMS_CSM1.0 model output prepared for CMIP6 CMIP 1pctCO2. Earth System Grid Federation, accessed 16 December 2021, https://doi.org/10.22033/ESGF/CMIP6.9701.

——, 2019c: CAMS CAMS_CSM1.0 model output prepared for CMIP6 CMIP piControl. Earth System Grid Federation, accessed 16 December 2021, https://doi.org/10.22033/ESGF/CMIP6.9797.

Seland, Ø., and Coauthors, 2019a: NCC NorESM2-LM model output prepared for CMIP6 CMIP piControl. Earth System Grid Federation, accessed 16 December 2021, https://doi.org/10.22033/ESGF/CMIP6.8217.

——, and Coauthors, 2019b: NCC NorESM2-LM model output prepared for CMIP6 CMIP abrupt-4xCO2. Earth System Grid Federation, accessed 16 December 2021, https://doi.org/10.22033/ESGF/CMIP6.7836.

——, and Coauthors, 2019c: NCC NorESM2-LM model output prepared for CMIP6 CMIP 1pctCO2. Earth System Grid Federation, accessed 16 December 2021, https://doi.org/10.22033/ESGF/CMIP6.7802.

Serreze, M. C., A. P. Barrett, J. C. Stroeve, D. N. Kindig, and M. M. Holland, 2009: The emergence of surface-based Arctic amplification. *Cryosphere*, **3**, 11–19, https://doi.org/10.5194/tc-3-11-2009.

Sévellec, F., A. V. Fedorov, and W. Liu, 2017: Arctic sea-ice decline weakens the Atlantic meridional overturning circulation. *Nat. Climate Change*, **7**, 604–610, https://doi.org/10.1038/nclimate3353.

Smeed, D. A., and Coauthors, 2014: Observed decline of the Atlantic meridional overturning circulation 2004–2012. *Ocean Sci.*, **10**, 29–38, https://doi.org/10.5194/os-10-29-2014.

——, and Coauthors, 2018: The North Atlantic Ocean is in a state of reduced overturning. *Geophys. Res. Lett.*, **45**, 1527–1533, https://doi.org/10.1002/2017GL076350.

Stouffer, R., 2019a: UA MCM-UA-1-0 model output prepared for CMIP6 CMIP 1pctCO2. Earth System Grid Federation, accessed 16 December 2021, https://doi.org/10.22033/ESGF/CMIP6.8881.

——, 2019b: UA MCM-UA-1-0 model output prepared for CMIP6 CMIP piControl. Earth System Grid Federation, accessed 16 December 2021, https://doi.org/10.22033/ESGF/CMIP6.8890.

——, 2019c: UA MCM-UA-1-0 model output prepared for CMIP6 CMIP abrupt-4xCO2. Earth System Grid Federation, accessed 16 December 2021, https://doi.org/10.22033/ESGF/CMIP6.8882.

Swart, N. C., and Coauthors, 2019a: CCCma CanESM5 model output prepared for CMIP6 CMIP abrupt-4xCO2. Earth System Grid Federation, accessed 16 December 2021, https://doi.org/10.22033/ESGF/CMIP6.3532.

——, and Coauthors, 2019b: CCCma CanESM5 model output prepared for CMIP6 CMIP piControl. Earth System Grid Federation, accessed 16 December 2021, https://doi.org/10.22033/ESGF/CMIP6.3673.

——, and Coauthors, 2019c: CCCma CanESM5 model output prepared for CMIP6 CMIP 1pctCO2. Earth System Grid Federation, accessed 16 December 2021, https://doi.org/10.22033/ESGF/CMIP6.3151.

Swingedouw, D., P. Braconnot, and O. Marti, 2006: Sensitivity of the Atlantic meridional overturning circulation to the melting from northern glaciers in climate change experiments. *Geophys. Res. Lett.*, **33**, L07711, https://doi.org/10.1029/2006GL025765

Tatebe, H., and M. Watanabe, 2018a: MIROC MIROC6 model output prepared for CMIP6 CMIP 1pctCO2. Earth System Grid Federation, accessed 16 December 2021, https://doi.org/10.22033/ESGF/CMIP6.5371.

——, and ——, 2018b: MIROC MIROC6 model output prepared for CMIP6 CMIP abrupt-4xCO2. Earth System Grid Federation, accessed 16 December 2021, https://doi.org/10.22033/ESGF/CMIP6.5411.

——, and ——, 2018c: MIROC MIROC6 model output prepared for CMIP6 CMIP piControl. Earth System Grid Federation,

accessed 16 December 2021, https://doi.org/10.22033/ESGF/CMIP6.5711.

Visbeck, M., 2007: Power of pull. *Nature*, **447**, 383, https://doi.org/10.1038/447383a.

Volodin, E., and Coauthors, 2019a: INM INM-CM4-8 model output prepared for CMIP6 CMIP 1pctCO2. Earth System Grid Federation, accessed 16 December 2021, https://doi.org/10.22033/ESGF/CMIP6.4928.

——, and Coauthors, 2019b: INM INM-CM4-8 model output prepared for CMIP6 CMIP abrupt-4xCO2. Earth System Grid Federation, accessed 16 December 2021, https://doi.org/10.22033/ESGF/CMIP6.4931.

——, and Coauthors, 2019c: INM INM-CM4-8 model output prepared for CMIP6 CMIP piControl. Earth System Grid Federation, accessed 16 December 2021, https://doi.org/10.22033/ESGF/CMIP6.5080.

Waldman, R., J. Hirschi, A. Voldoire, C. Cassou, and R. Msadek, 2021: Clarifying the relation between AMOC and thermal wind: Application to the centennial variability in a coupled climate model. *J. Phys. Oceanogr.*, **51**, 343–364, https://doi.org/10.1175/JPO-D-19-0284.1.

Wang, C. Z., L. P. Zhang, S. K. Lee, L. X. Wu, and C. R. Mechoso, 2014: A global perspective on CMIP5 climate model biases. *Nat. Climate Change*, **4**, 201–205, https://doi.org/10.1038/nclimate2118.

Weaver, A. J., C. M. Bitz, A. F. Fanning, and M. M. Holland, 1999: THERMOHALINE CIRCULATION: High-latitude phenomena and the difference between the Pacific and Atlantic. *Annu. Rev. Earth Planet. Sci.*, **27**, 231–285, https://doi.org/10.1146/annurev.earth.27.1.231.

——, and Coauthors, 2012: Stability of the Atlantic meridional overturning circulation: A model intercomparison. *Geophys. Res. Lett.*, **39**, L20709, https://doi.org/10.1029/2012GL053763.

Weijer, W., W. Cheng, O. A. Garuba, A. Hu, and B. T. Nadiga, 2020: CMIP6 models predict significant 21st century decline of the Atlantic meridional overturning circulation. *Geophys. Res. Lett.*, **47**, e2019GL086075, https://doi.org/10.1029/2019GL086075.

Wieners, K.-H., and Coauthors, 2019a: MPI-M MPI-ESM1.2-LR model output prepared for CMIP6 CMIP abrupt-4xCO2. Earth System Grid Federation, accessed 16 December 2021, https://doi.org/10.22033/ESGF/CMIP6.6459.

——, and Coauthors, 2019b: MPI-M MPI-ESM1.2-LR model output prepared for CMIP6 CMIP 1pctCO2. Earth System Grid Federation, accessed 16 December 2021, https://doi.org/10.22033/ESGF/CMIP6.6435.

——, and Coauthors, 2019c: MPI-M MPI-ESM1.2-LR model output prepared for CMIP6 CMIP piControl. Earth System Grid Federation, accessed 16 December 2021, https://doi.org/10.22033/ESGF/CMIP6.6675.

Winton, M., W. G. Anderson, T. L. Delworth, S. M. Griffies, W. J. Hurlin, and A. Rosati, 2014: Has coarse ocean resolution biased simulations of transient climate sensitivity? *Geophys. Res. Lett.*, **41**, 8522–8529, https://doi.org/10.1002/2014GL061523.

Worthington, E. L., B. I. Moat, D. A. Smeed, J. V. Mecking, R. Marsh, and G. D. Mccarthy, 2021: A 30-year reconstruction of the Atlantic meridional overturning circulation shows no decline. *Ocean Sci.*, **17**, 285–299, https://doi.org/10.5194/os-17-285-2021.

Wu, T., and Coauthors, 2018a: BCC BCC-CSM2MR model output prepared for CMIP6 CMIP 1pctCO2. Earth System Grid Federation, accessed 16 December 2021, https://doi.org/10.22033/ESGF/CMIP6.2833.

——, and Coauthors, 2018b: BCC BCC-CSM2MR model output prepared for CMIP6 CMIP abrupt-4xCO2. Earth System Grid Federation, accessed 16 December 2021, https://doi.org/10.22033/ESGF/CMIP6.2845.

——, and Coauthors, 2018c: BCC BCC-CSM2MR model output prepared for CMIP6 CMIP piControl. Earth System Grid Federation, accessed 16 December 2021, https://doi.org/10.22033/ESGF/CMIP6.3016.

Yeager, S. G., and J. I. Robson, 2017: Recent progress in understanding and predicting Atlantic decadal climate variability. *Curr. Climate Change Rep.*, **3**, 112–127, https://doi.org/10.1007/s40641-017-0064-z.

——, and Coauthors, 2021: An outsized role for the Labrador Sea in the multidecadal variability of the Atlantic overturning circulation. *Sci. Adv.*, **7**, eabh3592, https://doi.org/10.1126/sciadv.abh3592.

Yukimoto, S., and Coauthors, 2019a: MRI MRI-ESM2.0 model output prepared for CMIP6 CMIP 1pctCO2. Earth System Grid Federation, accessed 16 December 2021, https://doi.org/10.22033/ESGF/CMIP6.5356.

——, and Coauthors, 2019b: MRI MRI-ESM2.0 model output prepared for CMIP6 CMIP abrupt-4xCO2. Earth System Grid Federation, accessed 16 December 2021, https://doi.org/10.22033/ESGF/CMIP6.6755.

——, and Coauthors, 2019c: MRI MRI-ESM2.0 model output prepared for CMIP6 CMIP piControl. Earth System Grid Federation, accessed 16 December 2021, https://doi.org/10.22033/ESGF/CMIP6.6900.

Zhang, J., and Coauthors, 2018: BCC BCC-ESM1 model output prepared for CMIP6 CMIP piControl. Earth System Grid Federation, accessed 16 December 2021, https://doi.org/10.22033/ESGF/CMIP6.3017.

——, and Coauthors, 2019a: BCC BCC-ESM1 model output prepared for CMIP6 CMIP abrupt-4xCO2. Earth System Grid Federation, accessed 16 December 2021, https://doi.org/10.22033/ESGF/CMIP6.2846.

——, and Coauthors, 2019b: BCC BCC-ESM1 model output prepared for CMIP6 CMIP 1pctCO2. Earth System Grid Federation, accessed 16 December 2021, https://doi.org/10.22033/ESGF/CMIP6.2834.

Zhang, R., 2010: Latitudinal dependence of Atlantic meridional overturning circulation (AMOC) variations. *Geophys. Res. Lett.*, **37**, L16703, https://doi.org/10.1029/2010GL044474.

——, R. Sutton, G. Danabasoglu, Y.-O. Kwon, R. Marsh, S. G. Yeager, D. E. Amrhein, and C. M. Little, 2019: A review of the role of the Atlantic meridional overturning circulation in Atlantic multidecadal variability and associated climate impacts. *Rev. Geophys.*, **57**, 316–375, https://doi.org/10.1029/2019RG000644.

Zhao, J., and W. Johns, 2014: Wind-forced interannual variability of the Atlantic meridional overturning circulation at 26.5°N. *J. Geophys. Res. Oceans*, **119**, 2403–2419, https://doi.org/10.1002/2013JC009407.

Ziehn, T., and Coauthors, 2019a: CSIRO ACCESS-ESM1.5 model output prepared for CMIP6 CMIP abrupt-4xCO2. Earth System Grid Federation, accessed 16 December 2021, https://doi.org/10.22033/ESGF/CMIP6.4238.

——, and Coauthors, 2019b: CSIRO ACCESS-ESM1.5 model output prepared for CMIP6 CMIP piControl. Earth System Grid Federation, accessed 16 December 2021, https://doi.org/10.22033/ESGF/CMIP6.4312.

——, and Coauthors, 2019c: CSIRO ACCESS-ESM1.5 model output prepared for CMIP6 CMIP 1pctCO2. Earth System Grid Federation, accessed 16 December 2021, https://doi.org/10.22033/ESGF/CMIP6.4231.